



Measuring surface temperature of isolated neutron stars and related problems  
by Marcus Alton Teter

A dissertation submitted in partial fulfillment of the requirements for the degree of Doctor of  
Philosophy in Physics  
Montana State University  
© Copyright by Marcus Alton Teter (2001)

Abstract:

New and exciting results for measuring neutron star surface temperatures began with the successful launch of the Chandra X-ray observatory. Among these results are new detections of neutron star surface temperatures which have made it possible to seriously test neutron star thermal evolution theories. The important new temperature determination of the Vela pulsar (Pavlov, et al., 2001a) requires a non-standard cooling scenario to explain it.

Apart from this result, we have measured PSR B1055-52's surface temperature in this thesis, determining that it can be explained by standard cooling with heating. Our spectral fit of the combined data from ROSAT and Chandra have shown that a three component model, two thermal blackbodies and a non-thermal power-law, is required to explain the data. Furthermore, our phase resolved spectroscopy has begun to shed light on the geometry of the hot spot on PSR B1055-52's surface as well as the structure of the magnetospheric radiation. Also, there is strong evidence for a thermal distribution over its surface. Most importantly, the fact that PSR B1055-52 does not have a hydrogen atmosphere has been firmly established.

To reconcile these two key observations, on the Vela pulsar and PSR B1055-52, we tested neutron star cooling with neutrino processes including the Cooper pair neutrino emission process. Overall, it has been found that a phase change associated with pions being present in the cores of more massive neutron stars explains all current of the data. A transition from neutron matter to pion condensates in the central stellar core explains the difference between standard and non-standard cooling scenarios, because the superfluid suppression of pion cooling will reduce the emissivity of the pion direct URCA process substantially. A neutron star with a mass of 1.2M with a medium stiffness equation of state and a T72 type neutron superfluid models the standard cooling case well. A neutron star of 1.4M, with a pion core, with the same type of equation of state modified for pion matter and a modified E1-0.6 pion superfluid model is the best option for the non-standard case. The results also suggest that the equation of state for neutron stars may have to be stiffer than medium.

Furthermore, our observational results from two other sources, SGR 1900+14 and 1E1207.4-5209, have helped us to expand the understanding of isolated neutron stars. The Chandra observation of SGR 1900+14 has strengthened the case that it is a magnetar, as the pulsed fraction and the spectral fits suggest a blackbody plus power-law model is preferred. Also, our analysis of the Chandra data of 1E1207.4-5209 suggests that it should have a hydrogen atmosphere. Future observations will certainly give even better insight to both of these objects, as well as PSR B1055-52.

MEASURING SURFACE TEMPERATURE  
OF ISOLATED NEUTRON STARS AND  
RELATED PROBLEMS.

by

Marcus Alton Teter

A dissertation submitted in partial fulfillment  
of the requirements for the degree

of

Doctor of Philosophy

in

Physics

MONTANA STATE UNIVERSITY — BOZEMAN  
Bozeman, Montana

December 2001

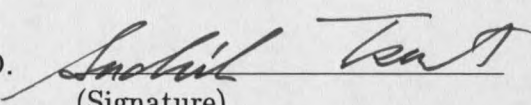
D378  
T291

APPROVAL

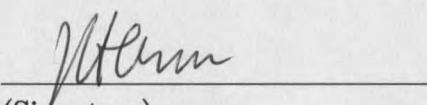
of a dissertation submitted by

Marcus Alton Teter

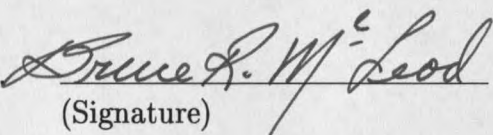
This dissertation has been read by each member of the dissertation committee, and has been found to be satisfactory regarding content, English usage, format, citations, bibliographic style and consistency, and is ready for submission to the College of Graduate Studies.

Sachiko Tsuruta, Ph. D.  12/3/2001  
(Signature) Date

Approved for the Department of Physics

John C. Hermanson, Ph. D.  12-3-01  
(Signature) Date

Approved for the College of Graduate Studies

Bruce R. McLeod, Ph. D.  12-10-01  
(Signature) Date

## STATEMENT OF PERMISSION TO USE

In presenting this dissertation in partial fulfillment of the requirements for a doctoral degree at Montana State University — Bozeman, I agree that the Library shall make it available to borrowers under rules of the Library. I further agree that copying of this thesis is allowable only for scholarly purposes, consistent with "fair use" as prescribed in the U. S. Copyright Law. Requests for extensive copying or reproduction of this thesis should be referred to University Microfilms International, 300 North Zeeb Road, Ann Arbor, Michigan, 48106, to whom I have granted "the exclusive right to reproduce and distribute my dissertation in and from microform along with the non-exclusive right to reproduce and distribute my abstract in any format in whole or in part."

Signature M. A. J. [Signature]

Date 3 DEC 2001

## ACKNOWLEDGEMENTS

I would like to thank Dr. G. Pavlov at The Pennsylvania State University department of Astronomy for his advise on the *Chandra* data analysis.

This research was sponsored in part by SAO grants GO0-1131A and GO0-1012X.

## TABLE OF CONTENTS

1	INTRODUCTION	1
2	CHANDRA X-RAY OBSERVATORY	12
	Introduction . . . . .	12
	Data Reduction . . . . .	14
3	CHANDRA OBSERVATION OF PSR B1055-52	20
	Introduction . . . . .	20
	Previous Observations and Results . . . . .	20
	Our <i>Chandra</i> Observation and Data Reduction . . . . .	24
	Our Results . . . . .	26
	One-Dimensional Spatial Results . . . . .	26
	Timing Results . . . . .	28
	Phase Integrated Spectral Analysis . . . . .	31
	Phase Resolved Spectroscopy . . . . .	41
	Discussion . . . . .	45
4	CHANDRA OBSERVATIONS OF SGR 1900+14	51
	Introduction . . . . .	51
	Magnetars . . . . .	51
	Soft Gamma-ray Repeaters(SGR) . . . . .	52
	Previous Outbursts of SGR 1900+14 . . . . .	53
	April 2001 Event . . . . .	54
	Our Results . . . . .	55
	Our Timing Results . . . . .	56
	Our Phase Integrated Spectral Analysis . . . . .	63

	Our Phase Resolved Spectral Analysis . . . . .	66
	Discussion . . . . .	68
5	CHANDRA OBSERVATIONS OF 1E1207.4-5209	72
	Introduction . . . . .	72
	Earlier Observations and Results . . . . .	73
	<i>Chandra</i> Observation and Previous Results . . . . .	73
	Our New Results from the <i>Chandra</i> Observation . . . . .	74
	Results of Our Timing Analysis . . . . .	75
	Results of Our Phase Integrated Spectral Analysis . . . . .	75
	Results of Our Phase Resolved Spectral Analysis . . . . .	78
	Discussion . . . . .	79
6	FUTURE OBSERVATIONS	83
	Future Missions . . . . .	83
	Future Observations of Neutron Stars . . . . .	83
7	COOPER PAIR NEUTRINO EMISSION AND COOLING OF NEUTRON STARS	86
	Introduction . . . . .	86
	Theoretical Background . . . . .	87
	Standard Neutrino Emission Mechanisms . . . . .	89
	Non-standard Neutrino Emission Mechanisms . . . . .	90
	Cooper Pair Neutrino Emission Mechanisms . . . . .	92
	Superfluid Models . . . . .	97
	Effects Upon Standard Cooling . . . . .	99
	Effects Upon Non-Standard Cooling . . . . .	101
	Discussion . . . . .	108
8	SUMMARY	114
	BIBLIOGRAPHY . . . . .	119

## LIST OF TABLES

1.1	List of isolated neutron star detections and a sample of upper limits. Numbered sources are detections, and lettered sources are upper limits.	5
1.2	Listing of standard and non-standard neutrino emission processes.	6
3.1	Summary of X-ray spectral results from previous observations. OF93 used <i>ROSAT</i> PSPC data only, while all others used a combined <i>ROSAT</i> PSPC and <i>ASCA</i> SIS data set.	23
3.2	Summary of X-ray spectral results from combined <i>ROSAT</i> and <i>Chandra</i> analysis using models from previous work. A single blackbody component is labeled as BB, and a single power-law component is labeled as PO. The hydrogen column density is $n_H$ . The soft blackbody apparent temperature are labeled $kT_S$ and radius $R_S$ . Similarly, the values for the hard blackbody are labeled with $kT_H$ and $R_H$ . The power-law index is $\Gamma$ , and the power-law normalization is $N_\Gamma$ . The fit statistic is $\chi^2$ , the degrees of freedom is d.o.f., and $\chi^2_\nu = \chi^2/\text{d.o.f.}$	33
3.3	Summary of X-ray spectral results from combined <i>ROSAT</i> and <i>Chandra</i> analysis using 3 component model.	36
3.4	Summary of X-ray spectral results from phase resolved <i>Chandra</i> analysis using 3 component model, case 1. The fixed parameters are $n_H=1.3 \times 10^{20} \text{ cm}^{-2}$ , $R_s=11.6$ km at 1 kpc, $kT_H=0.14$ keV, and $\Gamma=1.66$ .	42
3.5	Summary of X-ray spectral results from phase resolved <i>Chandra</i> analysis using 3 component model, case 2. The fixed parameters are $n_H=1.3 \times 10^{20} \text{ cm}^{-2}$ , $kT_s=72$ eV, $R_H=0.82$ km at 1 kpc, and $\Gamma=1.66$ .	42

4.1	Single power-law fit for both observations. The values in the parenthesis are best fit values using the fixed $n_{H,22}$ value from the combined fit. . . . .	64
4.2	Blackbody plus power-law fit for both observations. As before, the values in the parenthesis are for the best fit values using the fixed value for $n_{H,22}$ . . . . .	67
4.3	Phase resolved spectral results for power-law model with $n_{H,22}$ fixed at the phase integrated value of 2.85. . . . .	67

## LIST OF FIGURES

1.1	Standard cooling curve including the current detections (numbers) and upper limits (letters). See table 1.1 for description of the data. The standard cooling curve is for a $1.4M_{\odot}$ neutron star with an FP EOS and a T72 superfluid model. . . . .	4
2.1	<i>Chandra</i> CC mode image of 1E1207.4-5209 without correction for spacecraft dither and SIM motion. The image is a negative linear grey scale. The horizontal scale is position at $0''.5$ per pixel, and the vertical is time at 2.8 ms per pixel. . . . .	16
2.2	<i>Chandra</i> CC mode image of 1E1207.4-5209 with correction for spacecraft dither and SIM motion. . . . .	17
3.1	One dimensional continuous clocking (CC) mode image of PSR B1055-52. . . . .	27
3.2	$Z_1^2$ (Rayleigh) statistic as a function of frequency for the <i>Chandra</i> data set near the radio ephemeris. . . . .	29
3.3	Energy resolved light curves of the <i>Chandra</i> observation. . . . .	30
3.4	Pulsed fraction as a function of energy for the <i>Chandra</i> observation . . . . .	32
3.5	Results from PSR B1055-52 combined <i>ROSAT</i> and <i>Chandra</i> analysis using a two component model, two blackbodies. Notice the deviation of high energy photons in the residual. . . . .	34

- 3.6 PSR B1055-52 combined *ROSAT* and *Chandra* analysis using 2 component, blackbody plus power-law with fixed index,  $\Gamma=1.5$ . The distinctive sinusoidal distribution of the residuals indicate a poor fit. . . . . 35
- 3.7 Results from our PSR B1055-52 combined *ROSAT* PSPC and *Chandra* ACIS-S3 analysis using three component, two blackbodies plus power-law, model. The top panel shows the raw *ROSAT* (low energy) and *Chandra* (high energy) data sets. The middle panel shows the residual for the fit. The lower panel shows the unfolded spectra with telescope response taken into account. The 3 curves are the soft blackbody component (long dash), the hard blackbody component (dash), and the power-law component (dot). The sum of the three components is the solid line. . . . . 38
- 3.8 Confidence contours for soft blackbody for phase integrated spectrum. The contours are for  $n_{H,20}$  versus  $kT_S$  and  $R_S$  versus  $kT_S$ , where  $n_{H,20} = n_H / 10^{20} \text{ cm}^{-2}$  and  $R_S$  is the soft blackbody radius in km at 1 kpc. The contours are 1 (inner), 1.6 (middle) and  $2.6 \sigma$  (outer) using a 3 parameter fit. . . . . 39
- 3.9 Confidence contours for the hard blackbody and power-law normalization for the phase integrated spectrum. The contours are for  $N_\Gamma$  versus  $kT_H$  and  $R_H$  versus  $kT_H$ . Again, the contours are using a 3 parameter fit. . . . . 40
- 3.10 Phase resolved spectroscopy results case 1. The fixed parameters are labeled within the panels. The hydrogen column density,  $n_H$  was fixed at a value of  $1.3 \times 10^{20} \text{ cm}^{-2}$ . . . . . 43
- 3.11 Phase resolved spectroscopy results case 2. Again, the hydrogen column density,  $n_H$  was fixed at a value of  $1.3 \times 10^{20} \text{ cm}^{-2}$ . . . . . 44
- 3.12 Phase variation of blackbody bolometric fluxes (Case I). For the blackbody components the flux was computed by fixing the other parameters to their best fit values for each phase. The errors in the flux were estimated from a  $\chi^2_{min} + 1$  contour for the model component. The cgs units are  $\text{ergs s}^{-2} \text{ cm}^{-2}$ . . . . . 46
- 3.13 Phase variation of blackbody bolometric fluxes (Case II). See caption for figure 3.12 for details. . . . . 47

4.1	Comparison between first (top panel) and second (bottom panel) observation's $Z_1^2$ statistic. Both are compared to the best fit frequency for observation 1, $f_{0,1} = 0.1933143_{-1.3e-06}^{+1.0e-06}$ Hz. Note the slight shift for the second observation. . . . .	57
4.2	Light curve for the first <i>Chandra</i> observation. . . . .	58
4.3	Light curve for the second <i>Chandra</i> observation. . . . .	59
4.4	Energy resolved light curves for the first <i>Chandra</i> observation. There are insufficient counts below 1 keV and above 8 keV. . . . .	60
4.5	Energy resolved light curves for the second <i>Chandra</i> observation. The reduction of the observation time leads to an increase of uncertainty. . . . .	61
4.6	Energy resolved pulsed fraction for both of the <i>Chandra</i> observations. Notice the significant change in the 4-5 keV range. . . . .	63
4.7	Combined fit of both <i>Chandra</i> observations with a single power-law model. . . . .	65
4.8	Combined fit of both <i>Chandra</i> observations with a blackbody plus power-law model. . . . .	66
5.1	The spectrum of 1E1207.4-5209 <i>Chandra</i> data shows the absorption feature which prevented fitting. There is a large deviation in the residual in the range 1.2-1.5 keV. . . . .	76
5.2	Fit of absorption edge model for 1E1207.4-5209. The last data point shows the beginning of the background dominated region, but was ignored for fitting purposes. The edge can be seen in the top panel where the best fit line steps down. . . . .	78
5.3	Phase resolved spectral fits for 1E1207.4-5209 . The cgs units of flux is $\text{erg s}^{-1}\text{cm}^{-2}$ . The blackbody radius assumes a distance of 15 kpc. . . . .	80

7.1	Neutrino emissivity for neutron superfluidity of types A, B, and C. The superfluid critical temperature is chosen to be $T_n^{cr} = 10^9$ K, and the Cooper pair emission mechanism is shut down beyond $T_n^{cr}$ because of no superfluidity above the critical temperature. . . . .	95
7.2	Comparison between modified URCA and type B superfluid with superfluid critical temperature of $T_n^{cr} = 10^9$ K. . . . .	96
7.3	Comparison between several example superfluid models. For reference nuclear density is $2.8 \times 10^{14}$ (g cm <sup>-3</sup> ). The models with solid lines are for pions, while all others are neutron ${}^3P_2$ superfluids. . . . .	98
7.4	Standard cooling is shown for a $1.4M_\odot$ , FP EOS star with a T72 superfluid. The solid line is the standard cooling curve. The dashed line is the standard cooling including the Cooper pair neutrino emissivity. See figure 1.1 and table 1.1 for summary of data points. . . . .	101
7.5	Standard cooling is shown for a $1.4M_\odot$ star with a PS EOS and a T72 superfluid. The solid line is the standard cooling curve. The dashed line is the standard cooling including the Cooper pair neutrino emissivity. See figure 1.1 and table 1.1 for summary of data points. . . . .	102
7.6	Pion cooling with E1 superfluid model a $1.4M_\odot$ star with for the FP EOS. The dotted curve is for standard cooling for a star with $1.4M_\odot$ FP EOS and a T72 superfluid model without Cooper pair emission. The dashed curve is the E1 superfluid suppression for pion cooling with the LM factor $\tilde{g}' = 0.6$ without the Cooper pair effect. The solid curve includes the effect of Cooper pair neutrino emission on pion cooling. See figure 1.1 and table 1.1 for summary of data points. . . . .	107
7.7	Pion cooling with the modified E1 superfluid model a star with the pion FP EOS and $1.4M_\odot$ . The heavy solid curve is for standard cooling with a T72 superfluid and $1.2M_\odot$ , including Cooper pair emission. The other curves are for nonstandard (pion) cooling with the LM, $\tilde{g}' = 0.6$ . Each curve represents a different value of $\Delta T$ : dotted ( $\Delta T=0$ ), long dashed ( $\Delta T=0.2$ ), chain ( $\Delta T=0.4$ ), dashed ( $\Delta T=0.6$ ), and solid ( $\Delta T=0.8$ ). . . . .	109
7.8	Interior temperatures of non-standard and standard cooling as a function of internal density. The labels are the age in log (years). See text for explanation. . . . .	110

7.9 Comparisons between equations of state. The critical density for pions,  $\rho_{crit}$ , establishes the correct equation of state for neutron stars with masses near  $1.4M_{\odot}$ . EOSs become unstable when their masses begin to decrease with increasing density. . . . . 112

## ABSTRACT

New and exciting results for measuring neutron star surface temperatures began with the successful launch of the *Chandra* X-ray observatory. Among these results are new detections of neutron star surface temperatures which have made it possible to seriously test neutron star thermal evolution theories. The important new temperature determination of the Vela pulsar (Pavlov, et al., 2001a) requires a non-standard cooling scenario to explain it.

Apart from this result, we have measured PSR B1055-52's surface temperature in this thesis, determining that it can be explained by standard cooling with heating. Our spectral fit of the combined data from *ROSAT* and *Chandra* have shown that a three component model, two thermal blackbodies and an non-thermal power-law, is required to explain the data. Furthermore, our phase resolved spectroscopy has begun to shed light on the geometry of the hot spot on PSR B1055-52's surface as well as the structure of the magnetospheric radiation. Also, there is strong evidence for a thermal distribution over its surface. Most importantly, the fact that PSR B1055-52 does not have a hydrogen atmosphere has been firmly established.

To reconcile these two key observations, on the Vela pulsar and PSR B1055-52, we tested neutron star cooling with neutrino processes including the Cooper pair neutrino emission process. Overall, it has been found that a phase change associated with pions being present in the cores of more massive neutron stars explains all current of the data. A transition from neutron matter to pion condensates in the central stellar core explains the difference between standard and non-standard cooling scenarios, because the superfluid suppression of pion cooling will reduce the emissivity of the pion direct URCA process substantially. A neutron star with a mass of  $1.2M_{\odot}$  with a medium stiffness equation of state and a T72 type neutron superfluid models the standard cooling case well. A neutron star of  $1.4M_{\odot}$ , with a pion core, with the same type of equation of state modified for pion matter and a modified E1-0.6 pion superfluid model is the best option for the non-standard case. The results also suggest that the equation of state for neutron stars may have to be stiffer than medium.

Furthermore, our observational results from two other sources, SGR 1900+14 and 1E1207.4-5209, have helped us to expand the understanding of isolated neutron stars. The *Chandra* observation of SGR 1900+14 has strengthened the case that it is a magnetar, as the pulsed fraction and the spectral fits suggest a blackbody plus power-law model is preferred. Also, our analysis of the *Chandra* data of 1E1207.4-5209 suggests that it should have a hydrogen atmosphere. Future observations will certainly give even better insight to both of these objects, as well as PSR B1055-52.

## CHAPTER 1

## INTRODUCTION

The ability of measuring an isolated neutron star surface temperature has become a much easier task in recent years, because of the improvements in the orbiting observatories. The original *EINSTEIN* observatory, launched in 1978, gave the first indication of neutron star surface temperatures. It established upper temperature limits for many neutron stars, and created the first hope of beginning to reconcile theory with observation (e.g. Nomoto & Tsuruta 1981, 1986). Later, with the launch of *ROSAT*, the Röntgen Satellite developed mainly by Germany, the United States and the United Kingdom which was launched in 1990, three convincing detections were made for pulsars PSR B0656+14, PSR B1055-52, and Geminga. Afterwards, a few more neutron star's surface temperature measurements followed with the launch of *ASCA*, the fourth Japanese X-ray astronomy mission launched in 1993, and ground based optical telescopes. Finally, the introduction of *Chandra*, detailed in chapter 2, and *XMM-Newton*, the European Space agency's X-ray multi-mirror satellite, have improved the detection capabilities beyond all previous levels.

Neutron stars are thought to be born in supernova explosions. They are what

remains of the core of the progenitor star. If the core is above a certain mass, which remains uncertain but is estimated to be  $\sim 2-3M_{\odot}$ , the core will collapse into a black hole; otherwise, a neutron star is formed. The neutron star will begin life at extremely high temperatures, with core temperatures as high as  $\sim 10^{10-11}$  K, and cool off by various mechanisms.

The importance of detecting a neutron star's surface temperature relates to their thermal evolution. A neutron star first cools via various neutrino emission mechanisms, from the interior of the star, before the photon radiation from the surface becomes the dominant cooling process (Tsuruta, 1979). The first thermal evolution calculations (Tsuruta, 1964) showed that a neutron star should be visible as an X-ray source for about a million years. Among the important factors which seriously affect the nature of thermal evolution are the neutrino emission processes, the superfluidity of the core particles, the composition, and the mass of the neutron star.

The conventional neutrino cooling mechanisms, adopted in the earlier and most of the subsequent cooling calculations, such as the modified URCA, plasmon neutrino and bremsstrahlung processes, are called 'standard' cooling. On the other hand, the more exotic and extremely fast cooling processes, such as the URCA process involving pions, kaons, and quarks, and the direct URCA process involving nucleons and hyperons, are called 'nonstandard' processes (Tsuruta, 1998).

Once all neutrino cooling rates have decreased below the surface photon cooling rate, the photon cooling from the surface of the star takes over, dictating the remainder of the thermal evolution. Even though at earlier times the neutrino mechanisms

control the thermal evolution, the neutron star will emit photons from its surface. Consequently, through much of their earlier thermal history, neutron stars should remain visible as X-ray sources.

Measuring an isolated neutron star's temperature becomes important to test various thermal evolution theories. If a neutron star cools slowly through the standard cooling, its surface temperature will be higher than if it cools rapidly through non-standard cooling. Overall, early upper limits and detections showed that the standard cooling process would explain all the data, except for the Vela pulsar's upper limit. Later, as more observed temperatures became available, possible exceptions to standard cooling began to be discussed. Although, thermal evolution has been primarily a theoretical problem for many years, dating back to the nineteen-sixties (Tsuruta, 1964). It has only recently become a serious observational problem, with the addition of many more detections.

Figure 1.1 shows a typical standard cooling curve along with upper limits and detections of various isolated neutron stars. The upper limits shown here are mostly from *ROSAT* and combined *ROSAT* and *ASCA* observations. For RCW 103, both the upper limit based upon earlier *EINSTEIN* observation (c) and the new upper limit based upon new results (c\*) using *XMM-Newton* (Slane, 2001) are shown. In addition to the original three detections, PSR B1055-52 (6), PSR B0656+14 (4), and Geminga (5), additional new detections have been established. The new point, Vela (3) from the *Chandra* observation, together with the new RCW 103 upper limit (c\*) are the most important addition to the detection list, as its surface temperature

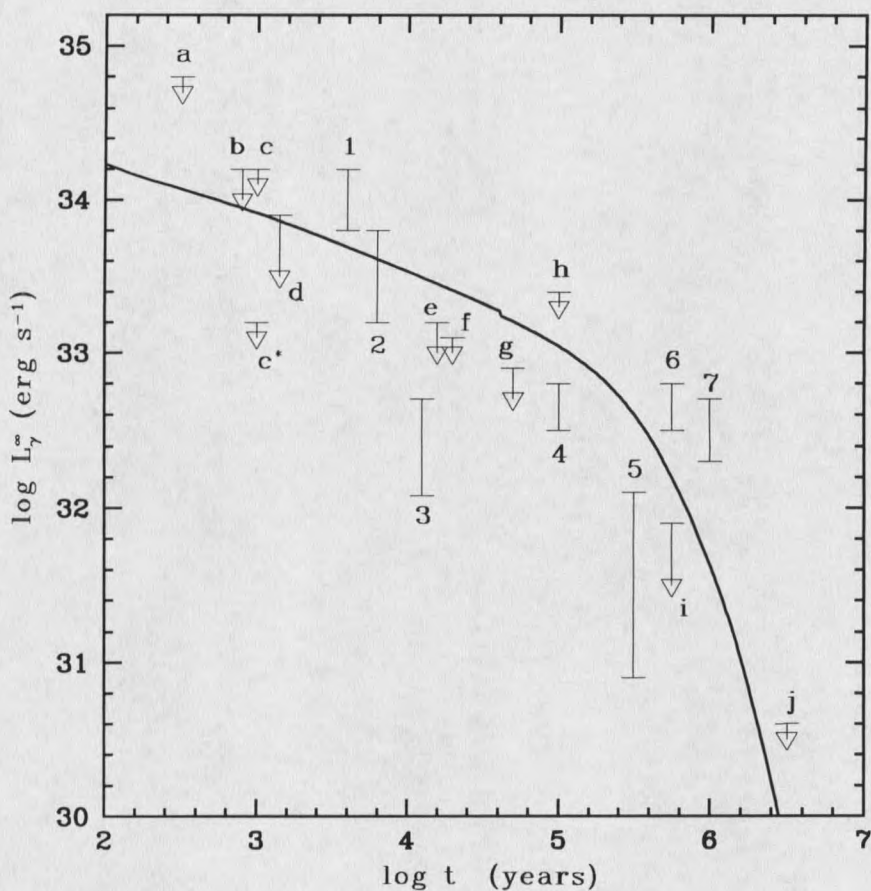


Figure 1.1: Standard cooling curve including the current detections (numbers) and upper limits (letters). See table 1.1 for description of the data. The standard cooling curve is for a  $1.4M_\odot$  neutron star with an FP EOS and a T72 superfluid model.

makes it an important candidate for non-standard cooling. The point source in Cas A (a), is included as an upper limit, even though the case for Cas A being a neutron star is far from certain (e.g. Pavlov et al, 2000, Umeda et al, 2000). Table 1.1 gives a summary of all the detections and upper limits.

The cooling curves are made using our 'exact' evolutionary code, where no isothermal approximation is made. This differs from isothermal codes because it includes the finite time scale of thermal conduction through the neutron star crust. The conduc-

Table 1.1: List of isolated neutron star detections and a sample of upper limits. Numbered sources are detections, and lettered sources are upper limits.

Source	Name	Reference
1	RX J0822-43	Zavlin, Trümper, & Pavlov, 1999
2	1E1207.4-5209	Zavlin, Pavlov & Trümper, 1998
3	Vela	Pavlov et al., 2001a
4	PSR B0656+14	Becker, 1995
5	Geminga	Becker, 1995
6	PSR B1055-52	Ögelman & Finley, 1993
7	PSR RX J185635-3754	Walter, Wolk, & Neuhäuser, 1996
a	Cas A point source	Pavlov et al., 2000
b	Crab pulsar	Becker, 1995
c	RCW 103	Tuohy & Garmire, 1980
c*	RCW 103	Slane, 2001
d	PSR B1509-58	Becker, 1995
e	PSR B1706-44	Becker, 1995
f	PSR B1823-13	Finley, Srinivasan, & Park, 1993
g	PSR B2234+61	Becker, 1995
h	PSR B1951+32	Becker, 1995
i	PSR B0355+54	Becker, 1995
j	PSR B1929+10	Becker, 1995

tion time scale depends upon the neutron star model of the equation of state (EOS) detailing the pressures associated with the strong nuclear force. For the softest EOS, BPS (Baym, Pethick & Sutherland, 1971), the conduction time scale is  $\sim 100$  years. For the FP (Friedman and Pandharipande, 1981) EOS, which is of medium stiffness, it is  $\sim 1000$  years. For the PS (Pandharipande, Pines & Smith, 1976) EOS, for stiff matter, it is up to  $\sim 10^4$  years. The cooling curves for the exact and the isothermal codes converge after those times. At present various neutron star EOSs are available (e.g. Wiringa, Fiks, & Fabrocini, 1988, and Nishizaki, Takatsuka, & Hiura, 1994), but we chose BPS, FP, and PS as representative EOSs for comparison to previous

results (e.g. Tsuruta, 1998).

Table 1.2 gives a listing of the standard and non-standard neutrino processes. The standard cooling is dominated by the modified URCA neutrino process (Friman

Table 1.2: Listing of standard and non-standard neutrino emission processes.

Standard	Non-standard
Modified URCA	Direct URCA (nucleons)
n-n bremsstrahlung	Pion URCA
n-p bremsstrahlung	Kaon URCA
plasmon neutrino	Hyperon URCA
Nuclear URCA	Quark URCA
$e^-$ -heavy ion bremsstrahlung	
$e^-e^+$ pair neutrino	
photo-neutrino	

and Maxwell, 1979, FM79 hereafter). The other processes are the neutron-neutron neutrino bremsstrahlung, neutron-proton neutrino bremsstrahlung (FM79), nuclear URCA (Tsuruta and Cameron, 1965), the electron-heavy ion neutrino bremsstrahlung (Itoh and Kohyama, 1984), and the plasmon neutrino, photo-neutrino, and electron-positron pair neutrino processes (Munakata et al., 1985). Overall, the modified URCA, and the neutron-neutron and neutron-proton neutrino bremsstrahlung processes in the central core produce the highest neutrino emissivity, though all of the standard cooling processes are accounted for in the cooling code used for this work. However, during the earliest stage of cooling when the information on the cooling in the central core has yet to be transmitted to the surface due to the finite time scale of thermal conduction, the surface cools due to the plasmon neutrino, the nuclear

URCA, and the electron-heavy ion bremsstrahlung processes operating in the inner crust.

The non-standard cooling has many options depending upon the composition of the core of a neutron star. By assuming the core is entirely nucleons with sufficiently high proton concentration, the validity of the direct URCA process for nucleons is pointed out (Lattimer et al., 1991). If the core is composed of pions, then the pion direct URCA process can take place (Muto, et al. 1988). Similarly, if kaons or quark matter is present, then corresponding kaon or quark direct URCA process is possible (Tatsumi, 1988 and Iwamoto, 1980).

To match the new observations, the choice of non-standard cooling has to be made; however, all of the non-standard cooling scenarios cool entirely too fast to be considered without some sort of suppression of their rates (e.g. Tsuruta, 1998). Fortunately, the core of neutron stars are expected to be in a superfluid state. Unlike terrestrial superfluids, under the ultra-high densities present in neutron star cores that are higher than the density of an atomic nucleus, the temperature is relatively high when core particles become superfluid. Typical superfluid critical temperatures,  $T_{cr}$ , below which superfluidity sets in, occurs in some cases at  $T_{cr} \sim 10^8$  K. Superfluid suppression of a non-standard neutrino emission mechanism slows the cooling rate such that non-standard cooling curves can approach the standard cooling curves. Some superfluid models have a very high  $T_{cr}$ , which essentially shuts down all the non-standard cooling process. Other superfluid models have  $T_{cr}$ s that are too low, which fail to suppress the non-standard cooling sufficiently to explain the data. The

challenge is to choose a superfluid model that has the right amount of suppression. Page (1990) began this exploration, showing cooling using various gap energies, and other authors have followed with improved physical models (e.g. Umeda, Tsuruta, & Nomoto, 1994, and Page, 1998).

From the observational standpoint, measurement of the relevant parameters has been improved with the newer generation of X-ray telescopes. First off, the distance to these objects has been difficult to measure. Using the fits for the observational data, there is a ratio of distance with some other parameter, which in turn is unknown. For example, a blackbody radiator model gives a normalization that is given by  $(R_S/d)^2$ , where  $R_S$  is the apparent effective radius at distance  $d$ . The apparent effective radius  $R_S$  relates to the real radius  $R$  by  $R_S = e^{-\phi_s/c^2} R$ , where  $e^{\phi_s/c^2} = (1 - 2GM/Rc^2)^{1/2}$  is the surface red-shift factor, with  $M$  being the gravitational mass and  $G$  the gravitational constant. Often, the distance to the neutron star is inferred from assuming that the effective radius is  $\sim 10$  km. Other methods of estimating the distance are also used to verify this assumption, but lacking a direct distance measurement will not constrain the radius. However, the availability of multi-wavelength observations and improved spectral resolution of X-ray telescopes have helped constrain the normalization by giving better distances and lowering the uncertainty.

Furthermore, getting the temperature has been improved. Often there are local areas of increased temperature, hot-spots (e.g. Greiveldinger, et al., 1996), which makes the model fitting more difficult since both the hot-spot and the stellar surface

have to be simultaneously fitted. With a sufficiently high number of measured X-ray photons, separating the two components has become increasingly easier with improved spectral resolution. Additionally, the magnetic fields associated with many neutron stars are thought to be very high,  $\sim 10^{12}$  Gauss for a typical pulsar. In such a high field, a magnetospheric pair plasma is thought to exist (e.g. Wang, et al., 1998). The non-thermal process involving this plasma does emit X-rays, so they also have to be considered when attempting to fit the data. Beyond this, there are also potential physical effects of the environment which might distort the direct measurement of the surface temperature; however, improved spatial resolution has helped to minimize this. The most notable is the effect of the interstellar medium. Neutral hydrogen absorbs radiation very efficiently in the ultraviolet range of energies, and this effect extends into the X-rays. Fitting the data requires including the effect of interstellar absorption, which can be constrained by multi-frequency observations.

Additionally, the neutron star's surface can modify the emitted radiation from a pure blackbody radiator. One of the most pronounced effects is that of an atmosphere (e.g. Romani, 1987). Fits of hydrogen atmosphere models have shown effective temperatures for several neutron stars that are lower than blackbodies (e.g. Pavlov et al., 1994). The most dramatic example of hydrogen atmosphere models is for the Vela pulsar, which has shown that its surface temperature is much lower and a radius that is much larger than what a blackbody model would predict (Pavlov et al., 2001a). Consequently, improvements in atmosphere models have made getting the effective temperature a much easier task.

If getting all of this information is difficult with just the X-ray spectrum, observational information from other wavelengths provides the clues to many of the challenges. For example, looking at the  $\gamma$ -ray energies will give clues about the magnetospheric radiation; furthermore, an optical and/or UV observation can also constrain the temperature as well as the magnetospheric radiation. Many of the isolated neutron stars also happen to be radio pulsars. Getting constraints on the rotation angles and magnetic axes from the radio observations give clearer pictures to the model that should fit the X-ray data. Periodic variation of X-rays from a pulsar allows timing analysis and production of light curves. *RXTE*, the Rossi X-ray timing explorer, which covers a higher X-ray energy band than does either *ROSAT* or *ASCA*, provides good timing information for brighter sources, as do *Chandra*'s capabilities. *Chandra* also provides the ability to begin the analysis of phase resolved spectroscopy which in turn should begin to put tighter constraints on the physical models.

In addition, observation has driven new theoretical considerations. The discovery of magnetars, isolated neutron stars with huge,  $\sim > 10^{14}$  Gauss magnetic fields, led to drastic modification to thermal evolution theories, since magnetar surface temperatures were far in excess of temperatures predicted by standard cooling of non-magnetized neutron stars. Several authors (e.g. Heyl and Hernquist, 1997) have done extensive work on the cooling of a magnetar. Though magnetar thermal evolution is an important theoretical consideration, it is beyond the scope of the cooling theory presented herein.

For the thermal evolution theory of isolated neutron stars, observation will estab-

lish the extents for the neutron star surface temperatures. The theoretical challenge will be establishing thermal evolution theory which explains all of the data in a concise physically reasonable way.

The scope of our work includes both the observational and theoretical challenges in part. Our work to measure neutron star surface temperature using one of the newest tools, the *Chandra* X-ray observatory, will be presented in chapters 3-5, while chapter 2 introduces *Chandra* and chapter 6 discusses briefly the future of neutron star observations. The *Chandra* observation of PSR B1055-52, in chapter 3, shows that the surface temperature remains about the same as previous *ROSAT* and *ASCA* results, but we found a three component model to be the best fit to the data, contrary to their two component models. In chapter 4, we show our results of the *Chandra* data analysis of SGR 1900+14 immediately following its most recent outburst, indicating that the magnetar model is a good explanation for the results. Chapter 5 shows our new spectral results of the *Chandra* data analysis of 1E1207.4-5209, indicating that a hydrogen atmosphere is required. Chapter 7 presents our results for the theoretical challenge offered by the new observations, with the effects of Cooper pair neutrino emissivity. We show that the correct choice of superfluid with pion cooling can explain all the currently available data. A summary, in chapter 8, will give the key observational and theoretical results.

## CHAPTER 2

## CHANDRA X-RAY OBSERVATORY

Introduction

The *Chandra* X-ray Observatory (CXO) was formerly known as AXAF, the Advanced X-ray Astrophysics Facility. Its capabilities were intended as a combination of the *ROSAT* and *ASCA* energy range with improved spatial and spectral resolution, with a larger effective area. The spatial resolution was accomplished by the combination of the high resolution mirror assembly (HRMA) combined with the small pixel size of the Advanced CCD Imaging Spectrometer (ACIS) and with the High Resolution Camera (HRC) chips. Spectral information is complemented by two gratings, the Low Energy Transmission Grating (LETG) and the *Chandra* High Energy Transmission Grating (HETG).

The HRMA is a set of four paraboloid-hyperboloid (Wolter-1) nested pairs that are 1.2 meters in diameter. The mirrors are grazing-incidence so that the X-rays do not penetrate deep into the mirror material before being reflected. The mirrors are coated with iridium to a depth of 30 nm. The effective area of the mirrors runs from

$\sim 800 \text{ cm}^2$  at 0.5 keV and drops down to  $\sim 400 \text{ cm}^2$  at 2.0 keV, then steadily drops off at higher energies. The large effective area of the mirror make the spatial and spectral resolution the best yet made.

At the rear of the telescope in the focal plane is the Scientific Instrument Module (SIM). The SIM contains the ACIS and HRC chips along with the LETG and HETG gratings. The various instruments can be brought into focus and can be used for observations depending upon the scientific objectives.

The ACIS is an array of 10 CCDs. Four of the CCDs are designed especially for imaging, being designated the ACIS-I. They are arranged in a square, 2 x 2 array, at the center of the focal plane. Below the ACIS-I on the focal plane, are the 6 ACIS-S CCDs, designed for spectral work in imaging mode or with one of the two gratings. Two of the CCDs are back illuminated, while the other 8 are front illuminated. The ACIS CCDs have excellent spatial resolution,  $\sim 0.5$  full width half maximum (fwhm). The timing resolution is  $\sim 3$  s in imaging mode; however, the ACIS-S3 can be used in Continuous Clocking (CC) mode, improving the timing resolution to  $\sim 3$  ms, but the image is reduced to 1 dimension.

The HETG is the principle grating to be used with the ACIS-S CCD array. The grating is composed of two gratings for high and medium energies, the High Energy Grating (HEG) and the Medium Energy Grating (MEG). The HEG and MEG are offset from each other on the ACIS array to avoid overlap so that the spectral information can be used simultaneously.

The HRC consists of a set of two Micro-Channel Plate (MCP) type detectors. One

is optimized for imaging (HRC-I) and the other is a readout for the LETG (HRC-S). The HRC-I has the largest field of view of all of *Chandra* instruments giving a half degree by half degree image. The spatial resolution of the HRC detectors are  $\sim 0''.4$  fwhm. The spectral range for the HRC is larger than that of the ACIS, but the spectral resolution is much less for the HRC-I. The timing resolution of the HRC is the best available on *Chandra*, having 16  $\mu$ s resolution.

The LETG is the grating for the HRC-S detector, though it can be used with the ACIS-S array. The energy range with the HRC-S is 70-7290 eV and 200-8860 eV with the ACIS-S. The resolution for a spectral line in these ranges is  $\sim 0.005$  nm fwhm, having the highest resolving power available on *Chandra* at low energies (0.08-0.2keV). The LETG in combination with the HRC-S allows time resolved spectra and spatially resolved spectra of multiple sources (*Chandra* Proposers Observatory Guide, 2000).

### Data Reduction

The data reduction for *Chandra* is an involved process for each of the different instruments and modes available. Since our work primarily involves the use of the ACIS-S3 chip in CC mode without any gratings, the discussion will be confined to procedures for that chip and mode. Similar procedures can be used for the ACIS in imaging mode. The analysis is performed using utilities from the *Chandra Interactive Analysis of Observations* (CIAO) software package, available from the *Chandra X-*

ray Center (CXC), and the xspec spectral analysis program, available from the High Energy Astrophysics Science Archive Research Center (HEASARC).

The raw data received by the CXC at Harvard University, is first run through some pre-processing, called pipeline processing, before being made available to the individual observers. This procedure sets up the data in a usable form for the user. The raw data, without any pipeline processing, is available, but its use is not recommended. Bias correction, overclock correction and coordinate transformations are applied to the data in this process. Also, any events which are certain to be considered bad due to background flares or solar activity are removed. Once the processing pipeline has been produced, the data is made available to the users (Data Products Guide, 2001).

The first important procedure that we must perform is to correct the observation for spacecraft dither and SIM motion. This affects the position and the time of the event, because the y-axes of the chip is used to compute time. Figure 2.1 shows the raw event file prior to the correction. Without the correction, the timing analysis is flawed, producing several periods near the actual period, and spectral analysis has a potential for flaws, because of the increased background. Correcting for this motion requires applying the following correction:

$$t_{corr} = t + t_o \sin\xi (\alpha - \alpha_{med}) \cos\delta_{med} - t_o \cos\xi (\delta - \delta_{med}), \quad (2.1)$$

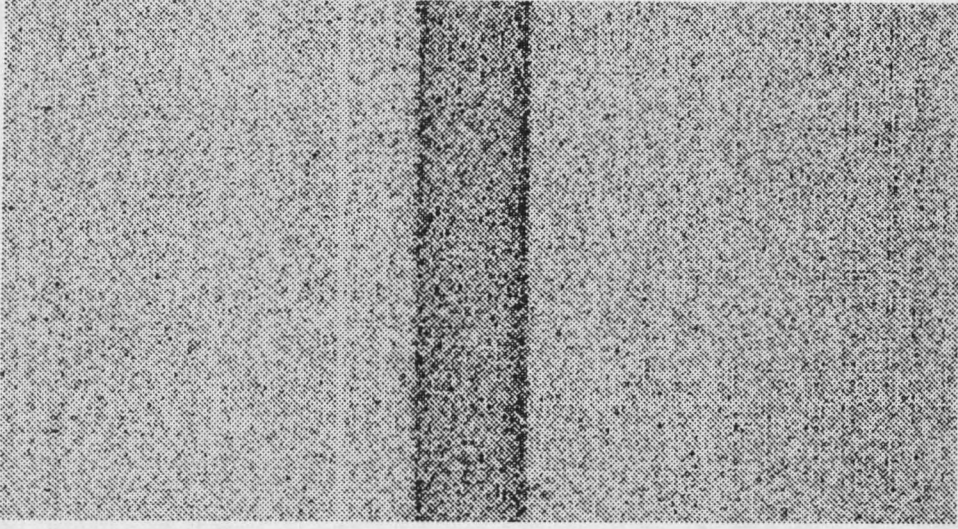


Figure 2.1: *Chandra* CC mode image of 1E1207.4-5209 without correction for spacecraft dither and SIM motion. The image is a negative linear grey scale. The horizontal scale is position at  $0''.5$  per pixel, and the vertical is time at 2.8 ms per pixel.

and

$$x_{corr} = x + x_o \cos\xi (\alpha - \alpha_{med}) \cos\delta_{med} - x_o \sin\xi (\delta - \delta_{med}), \quad (2.2)$$

where  $t$  is the spacecraft time,  $t_o = 20.857898$  s,  $x_o = 7318.5607$  pixels,  $\alpha_{med}$  and  $\delta_{med}$  are the median right ascension and declination for the spacecraft throughout the observation. Furthermore,  $\xi$ ,  $\alpha$ , and  $\delta$ , are the spacecraft roll angle, right ascension, and declination of the spacecraft at the time of the event (Allen, 2000). Figure 2.2 shows the CC mode image after the appropriate corrections have been applied.

After corrections for the dither and SIM motion, the times must be corrected for accurate timing analysis. To get accurate timing analysis all motions of the spacecraft have to be taken into account and the resulting arrival times need to be computed with respect to a common reference point. The accepted reference is to compute the

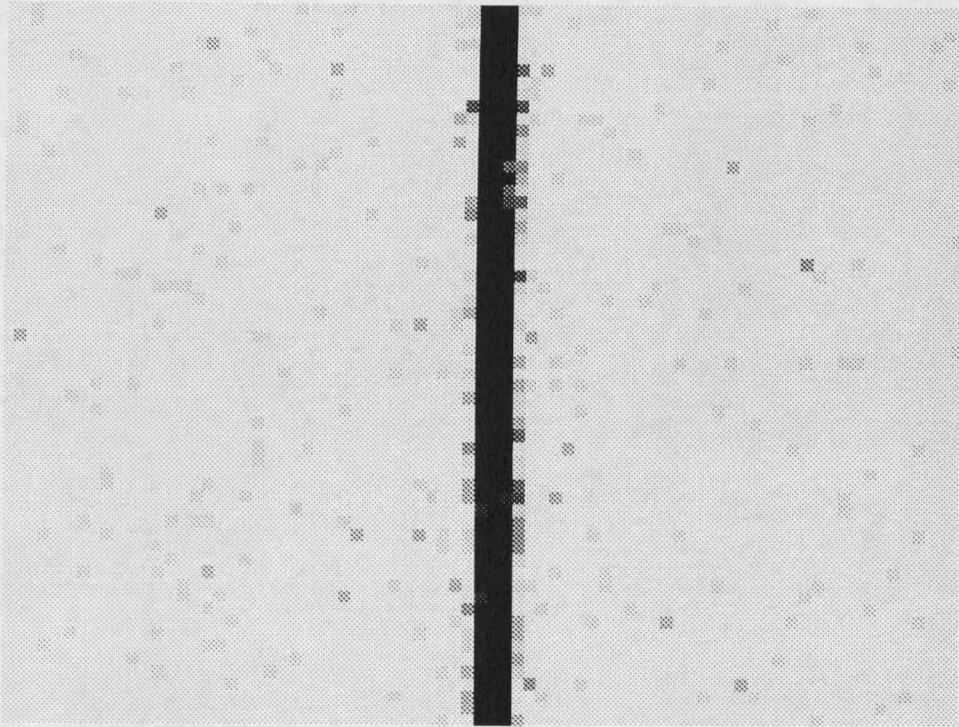


Figure 2.2: *Chandra* CC mode image of 1E1207.4-5209 with correction for spacecraft dither and SIM motion.

arrival times with respect to the solar system barycenter. This is accomplished using the *AxBary* utility provided with the CIAO software package. Once these important corrections have been made, the data is ready to be used for scientific analysis.

The CIAO package provides many tools for manipulating the data, the four most useful tools in pulsar data analysis are *dmlist*, *dmcopy*, *dmextract*, and *dmstat*. All of the tools have the ability to apply filters to the data files. The filtering can be done versus any column in the data file. It can be a spatial filter, removing contributions from all but a certain region of the chip, a timing filter, getting times of interest, or many others. The tool *dmlist* allows listing of the contents of a data file, providing

a quick way to write needed information to an ASCII text file. To copy the filtered contents from one data file to another, the tool `dmcopy` is useful. Extracting spectral information for use with `xspec` is accomplished using `dmextract`. Lastly, the tool `dmstat` gives the maximum, minimum, and mean values of specified columns in the data set.

The filtering allows a very small area to be determined as the source, while a wider area can be established as the background. Copying the source and backgrounds into separate files, further analysis can be easily achieved. The bulk of the source counts is typically in a one or two pixel width area in a CC mode image. The sources were extracted including a one or two pixel tail on either side of the source. Backgrounds were about five times the width of the source extraction, to account for the lower background count rates.

Timing analysis is accomplished by writing the source event times to a data file and then running various programs to determine the period and light curves. Once the period is determined, the phase of each photon can be determined easily. This information can be written back into the data file with use of many different utilities.

Spectral analysis was accomplished by extracting spectral files for both the source and background. Fitting of the spectra were all accomplished by use of the `xspec` program. Often, part of the spectrum was ignored during fitting. There are reasons for this. First, data above a certain energy is noisy because of the background beginning to dominate. Before any spectral fitting was done to any spectrum, background and source spectra were compared to see at what energy the background begins to

dominate. All source counts above that energy were rejected. Second, the spectral response of the telescope itself is still unknown in certain energy ranges. As of this writing, there is reason for a high uncertainty for the spectral responses below 0.5 keV. Determining accurate responses are difficult for this range because of a lack of spectral lines for calibration in this range.

## CHAPTER 3

### *CHANDRA* OBSERVATION OF PSR B1055-52

#### Introduction

PSR B1055-52 is especially interesting for this thesis because it is one of the three isolated radio pulsars whose surface radiation was detected by *ROSAT*, and because it is, together with SGR 1900+14 and 1E1207.4-5209, presented in chapters 4 and 5, one of the three X-ray sources whose *Chandra* data were analyzed by the author.

#### Previous Observations and Results

PSR B1055-52 is one of the earliest discovered radio pulsars. It was discovered by Vaughan & Large in 1972 and has been extensively monitored in the radio wavelengths. Furthermore, it was one of the targets observed by the Compton Gamma Ray Observatory (CGRO) (Kaspi 1994, D'Amico et al 1996). Recently, the Hubble Space Telescope (HST) managed to image the pulsar despite the bright stars within the field of view that had made previous ground based observations impossible. PSR B1055-52 has also been observed in the X-ray band, by *ROSAT*, *ASCA*, and *RXTE*.

Very recently, it has been a target of *Chandra* and *XMM-Newton*.

The radio observations of PSR B1055-52 have given a radio pulse profile consisting of a pulse and inter-pulse separated by  $120^\circ$  in phase (Biggs 1990). Lynn & Manchester (1988) extensively modeled many radio pulsars and found that the polarization position angle from the magnetic poles leads to an angle between the rotation and magnetic axes to be  $\sim 75^\circ$  for PSR B1055-52. Observations and modeling of the radio data have suggested that PSR B1055-52 rotates at an oblique angle between the rotation axes and the observation axes, of  $\gamma \sim 65^\circ$ . The pulse and inter-pulse, that are consistent from 60 MHz to 1.4 GHz, are naturally explained as beamed radiation from opposite poles of the magnetic field sweeping past the observer.

At the opposite end of the electromagnetic spectrum, the  $\gamma$ -ray observations of PSR B1055-52 have been extensive. It is one of at least seven spin-powered pulsars that have been detected at  $\gamma$ -ray energies (Fierro et al. 1993). Between 1991 and 1998, it was observed by CGRO, giving details of the pulsed  $\gamma$ -ray radiation (Ulmer 1994, Thompson et al. 1999). The important results are: (i) a main peak in phase with the radio, with a secondary peak that is 0.2 separated in phase, (ii) the  $\gamma$ -ray flux does not vary over large time scales, (iii) the energy spectrum is power-law with index  $\Gamma = 1.58 \pm 0.15$ , from  $\sim 70 - 1000$  MeV, and a break above 1000 MeV to an index of  $\Gamma = 2.04 \pm 0.30$ , and (iv) the observed  $\gamma$ -ray radiation represents 6 - 13% of the spin down luminosity, depending upon unknown beaming geometry and uncertain distance. The OSSE (48 - 184 keV) and COMPTEL (0.75 - 30 MeV)  $\gamma$ -ray light curves are noisy with only a visible pulse in the COMPTEL range; however, the

EGRET ( $> 240$  MeV)  $\gamma$ -ray light curve has a narrow pulse width and two distinct peaks.

The optical/UV observation of PSR B1055-52 used HST (Mignani et al., 1997). The Faint Object Camera (FOC) observation using the U(F342) filter gave a magnitude of  $m_{F342} = 24.88 \pm 0.1$ , corresponding to a flux of  $1.3 \times 10^{-30}$  ergs  $\text{cm}^{-2}$   $\text{s}^{-1}$   $\text{Hz}^{-1}$ . We found the optical data point to lie upon a continuous power-law of index  $\Gamma = 1.47$ , from the  $\gamma$ -ray range, indicating that the optical and the  $\gamma$ -ray are both magnetospheric in origin. Furthermore, the optical flux is not consistent with the blackbody emission, as all reasonable temperatures and normalizations established from X-ray observation give a flux in the optical that is too low, indicating to us that the optical includes a magnetospheric component.

X-ray observations have been carried out by several satellites. Early observations included *EINSTEIN* (Cheng and Helfand 1983) and *EXOSAT* (Brinkman and Ögelman 1987) but were limited by poor statistics. The first significant observation was carried out in 1992 by Ögelman and Finley (1993, hereafter OF93) using *ROSAT* PSPC and HRI detectors. Later, *ASCA* observed PSR B1055-52 (Greiveldinger et al. 1996, hereafter G96), but poor spatial resolution and a low number of counts limited the results.

The spectral analysis of the *ROSAT* and *ASCA* observations are summarized in table 3.1. OF93 found that a single blackbody model fits the data to an energy of 0.7 keV but leaves significant residuals at higher energies. Their single power-law model fits the data well at all energies, but it would imply an optical flux far in excess of the

Table 3.1: Summary of X-ray spectral results from previous observations. OF93 used *ROSAT* PSPC data only, while all others used a combined *ROSAT* PSPC and *ASCA* SIS data set.

Model	$n_H$ $\times 10^{20} \text{ cm}^{-2}$	Model Parameter	flux $\text{keV cm}^{-2} \text{ s}^{-1}$	Ref.
Blackbody	$2.4 \pm 0.8$	$kT = 70 \pm 5 \text{ eV}$	$(4.8 \pm 1.2) \times 10^{-3}$	OF93
Power-law	$5.7 \pm 1.0$	$\Gamma = 5.8 \pm 0.5$	$(1.9 \pm 0.9) \times 10^{-1}$	OF93
Blackbody(soft) plus Blackbody(hard)	$3.5 \pm 1.0$	$kT_s = 60 \pm 5 \text{ eV}$ $kT_h = 200 \pm 100 \text{ eV}$	$(8 \pm 2) \times 10^{-3}$ $(1.2 \pm 0.7) \times 10^{-3}$	OF93
Blackbody(soft) plus Blackbody(hard)	$2.6 \pm 0.6$	$kT_s = 68_{-9}^{+5} \text{ eV}$ $kT_h = 320_{-100}^{+170} \text{ eV}$	$3.8_{-0.1}^{+0.4} \times 10^{-2}$ $6.2_{-1.9}^{+4.4} \times 10^{-5}$	G96
Blackbody(soft) plus Power-law(hard)	$3.0 \pm 1.0$	$kT_s = 60 \pm 5 \text{ eV}$ $\Gamma = 1.4 - 1.5$	$(7 \pm 2) \times 10^{-3}$ $(3 \pm 2) \times 10^{-5}$	OF93
Blackbody(soft) plus Power-law(hard)	...	$T_s = 68_{-9}^{+5} \text{ eV}$ $\Gamma = 1.5 \pm 0.3$	$1.4 \times 10^{-2}$ $9.8 \times 10^{-5}$	W98

HST measurement. Furthermore, the light curves for the observation indicate that a single spectral component can not explain the data. Two component fits for *ROSAT* PSPC and *ROSAT* PSPC with *ASCA* SIS show that blackbody plus power-law and two blackbody models fit the data equally well (OF93), though G96 preferred the two blackbody model and Wang et al. (1998, hereafter W98) preferred the blackbody plus power-law model for separate reasons.

The timing analysis of the *ROSAT* observation of PSR B1055-52 has shown clearly at least two components. At energies lower than 0.5 keV, the light curve is broad and has a small pulse fraction of 0.1. At higher energies, above 0.5 keV, the light curve is narrower. At 0.5 keV the pulse fraction increases to nearly 0.8 at approximately

1.0 keV then decreases again. The higher energy peak is phase shifted by  $110^\circ$  from the low energy peak (OF93). Though the *ROSAT* low energy peak has been reported to be in phase with the radio, the result has not been able to be duplicated by subsequent investigation (Pavlov et al., 2001b). There are two reasons for this: (i) the *ROSAT* orbit information during the period of the observation is unknown, requiring an extrapolation of the orbit from earlier and later times when it is known, and (ii) the original *ROSAT* data set has been subsequently reprocessed to modern data formats in 1995, so it is uncertain if the timing information has been modified from the original 1993 data set. However, the relative phase of the *ROSAT* light curves are verified by the *Chandra* light curves (see *Chandra* timing analysis).

#### Our *Chandra* Observation and Data Reduction

We observed PSR B1055-52 with *Chandra*'s ACIS-S3 chip in continuous clocking (CC) mode on 5 January 2000 for a total of 39.9 ks, giving approximately 27000 counts from the pulsar. CC mode has a timing resolution of 2.85 ms, but sacrifices one dimension of spatial information for timing, leaving one dimensional spatial information. The photon arrival times and sky positions had not been corrected for spacecraft dither and the SIM motion at the CXC, so we made manual corrections for these (Allen 2000, Tenant 2001).

The one dimensional nature of the CC observation required special handling to determine the background, spectral response, and telescope ancillary response. First

off, by studying the *ROSAT* HRI image of the field of view, taking into account the *Chandra* orientation for the observation, we found no point sources near PSR B1055-52 that would contribute to the source; however, it would have been ideal to use a *Chandra* HRC to image the field for faint sources that *ROSAT* would not have been able to detect, but none was available. We assumed the background to be a contribution of the entire column of the ACIS-S3 chip along the source position; consequently, we chose a wide set of columns near the source position as the background. Even though the spectral response and the ancillary response are not necessarily the same along the column, the background subtraction will remove the unwanted counts from the source since the background is equally affected by the change of spectral and ancillary response. For the spectral and ancillary response, we determined the aim point for the observation and verified the location of the source upon the chip was verified by its 'chipx' coordinate and the roll angle for the spacecraft. The spectral and ancillary response were chosen specifically for this location on the chip, which is exactly the procedure used to determine the responses for a point source for the ACIS-S3 chip in imaging mode.

Once the source, background, and responses were chosen, a 1-D image, light curves, and spectra were made and analyzed. We also made phase resolved spectra by calculating the phase of each arriving photon and sorting the data according to phase (see results section for details).

As of this writing, the spectral responses for *Chandra* ACIS-S3 below 0.5 keV are unknown. The reason for the difficulty is the lack of spectral lines in this range to

calibrate the detector. Rather than attempting to correct the *Chandra* responses, we used the data set from the *ROSAT* PSPC observation for spectral analysis for the low energy range. The 1-D image and light curves were unaffected by the uncertainty. Since *ROSAT* PSPC timing information remains uncertain, only *Chandra* data set was used for phase resolved spectroscopy (Pavlov et al, 2001b).

### Our Results

Our goals for the analysis of the PSR B1055-52 *Chandra* data involved several things. First, we would search the one-dimensional image for evidence of a compact nebula. Furthermore, we wanted to carry out a detailed timing analysis including energy resolved light curves and pulsed fractions. Next, we would embark on a detailed spectral analysis to resolve the discrepancy between the differing interpretations of G96 and W98 for the combined *ROSAT* and *ASCA* observations. Lastly, we would begin a phase resolved spectral analysis to constrain the geometry of the spectral components. In the following subsections, we present our results.

#### One-Dimensional Spatial Results

The one dimensional image, figure 3.1, shows the number of counts versus the chip  $x$  position on the ACIS-S3. The peak at chip pixel 294 has 6376 raw pulsar counts. The plot has been fit to a Gaussian curve that has a full-width-half-maximum (fwhm) of approximately 1 pixel, or  $0''.5$ , confirming the ACIS-S3 resolution. A point source

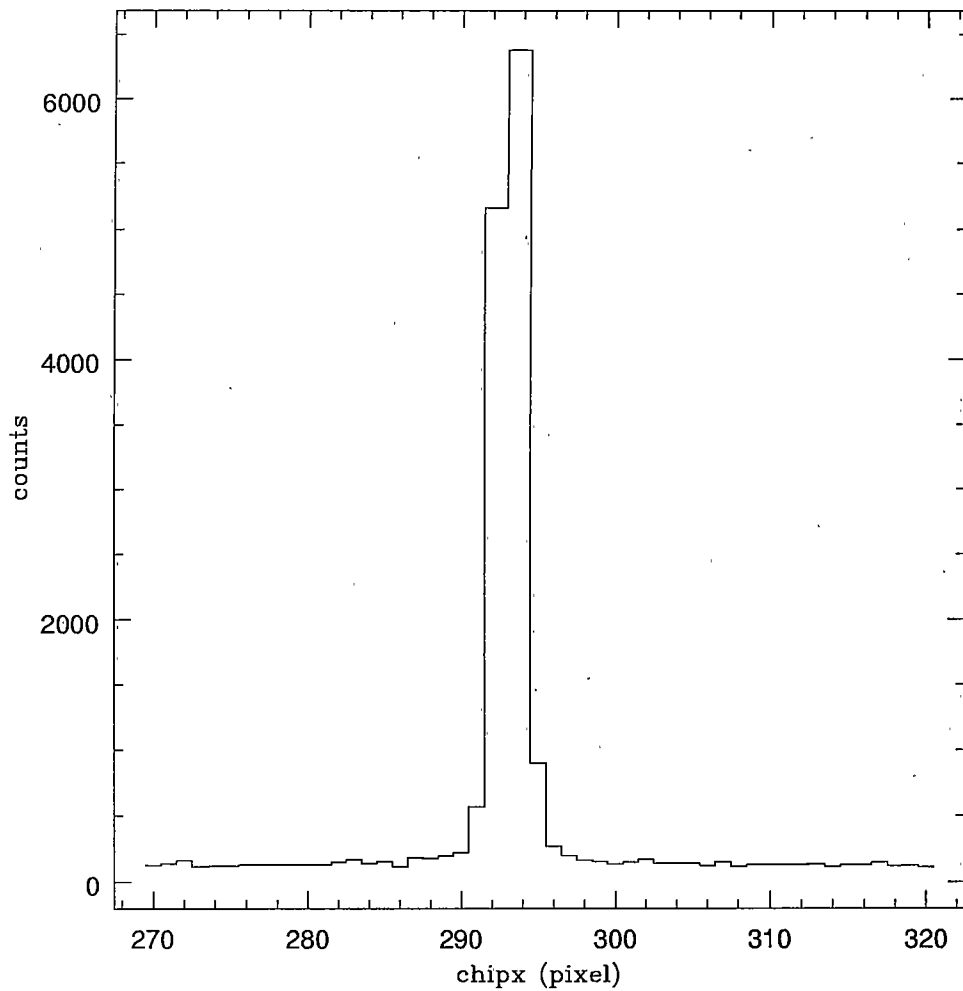


Figure 3.1: One dimensional continuous clocking (CC) mode image of PSR B1055-52.

should only be approximately 1 pixel wide.

The width of the tails in figure 3.1 suggests that there might be a compact nebula around PSR B1055-52, because of the increased counts that are at the base of our best fit Gaussian; however, the low number of counts and the high CC mode background made it impossible to prove. Hopefully, a high resolution image will be attempted at sometime in the future since the existence of compact nebulae around pulsars has

become an important topic because of the rich structure found in the compact nebula surrounding the Vela pulsar (Pavlov et al., 2001a).

### Timing Results

We corrected the times to the solar system barycenter using the `axBary` utility which directly accounts for the spacecraft orbit and the orbit of the various bodies in the solar system, using the period and period derivative for PSR B1055-52 taken from the radio ephemeris of the Australian Pulsar Timing Archive. Careful analysis of the delay between the photon arriving on the ACIS-S3 chip and the time when the photon would be read out, allowed the computation of the phase of all X-ray photons with respect to the radio phase.

We checked the period of the *Chandra* data by examining the arrival times for periodicity near the radio ephemeris. The  $Z_1^2$  (Rayleigh) test was used. Figure 3.2 shows the strong peak at 5.0732672 Hz, which is consistent with the radio ephemeris. The variable  $Z_1^2$  has a probability density function equal to that of  $\chi^2$  with 2 degrees of freedom, thus obtaining a noise peak by chance in one trial is  $\exp(-Z_1^2/2)$ . Consequently, for  $N$  independent trials the probability is  $\rho = N \exp(-Z_1^2/2)$  (Zavlin, et al, 2000). At the peak,  $Z_1^2 = 462.220088$ , so for one trial the probability for obtaining such a peak by chance is  $\sim \exp(-231.11)$ . Consequently, we find a confidence,  $C = (1 - \rho) \times 100\%$ , for such a peak being the actual period of pulsations is nearly 100%.

Our light curves with respect to the radio phase are presented in figure 3.3. We

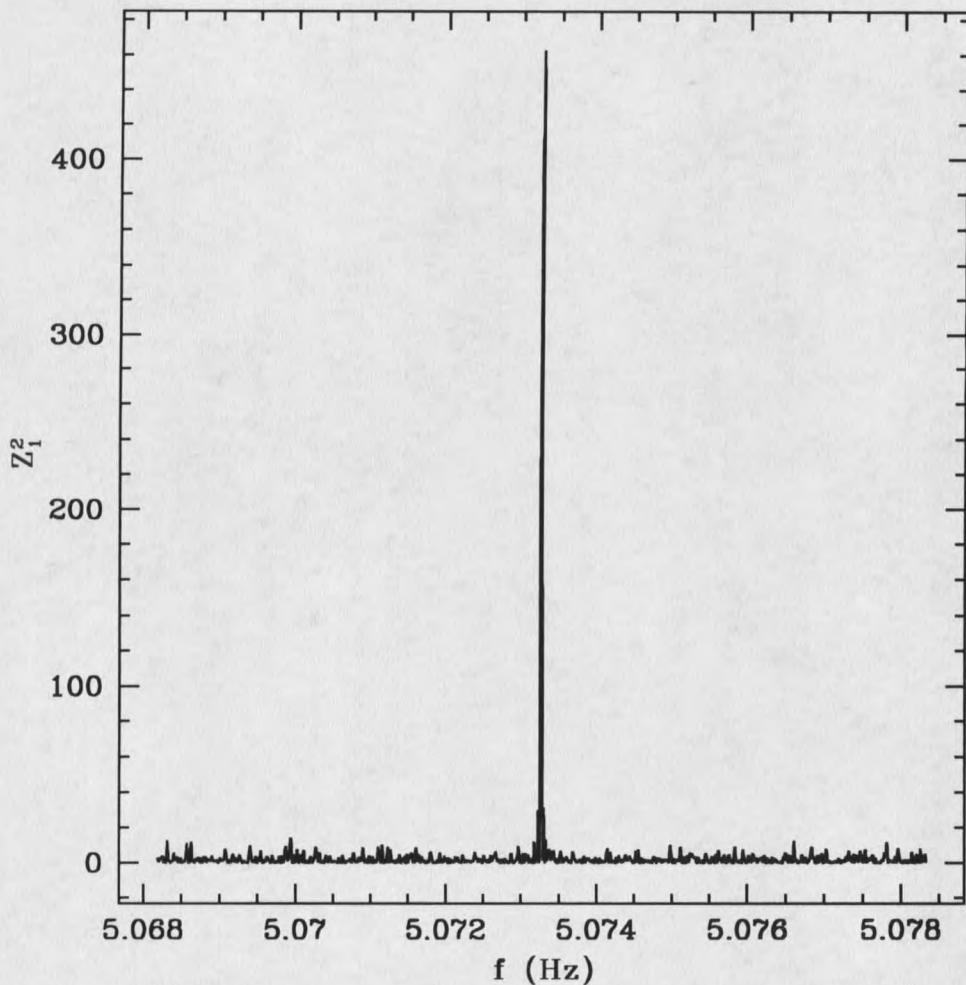


Figure 3.2:  $Z_1^2$  (Rayleigh) statistic as a function of frequency for the *Chandra* data set near the radio ephemeris.

present the light curves using ten phase bins for the benefit of reader, while our analysis was performed using twenty phase bins and artificially smoothed light curves. Overall, they are very similar to the *ROSAT* light curves from OF93; however, the absolute phase of the *Chandra* light curves are different from those for *ROSAT*. The reason is because of the unknown orbit information for *ROSAT* during its observation of PSR B1055-52. The *Chandra* light curve is broad at low energy but narrows at

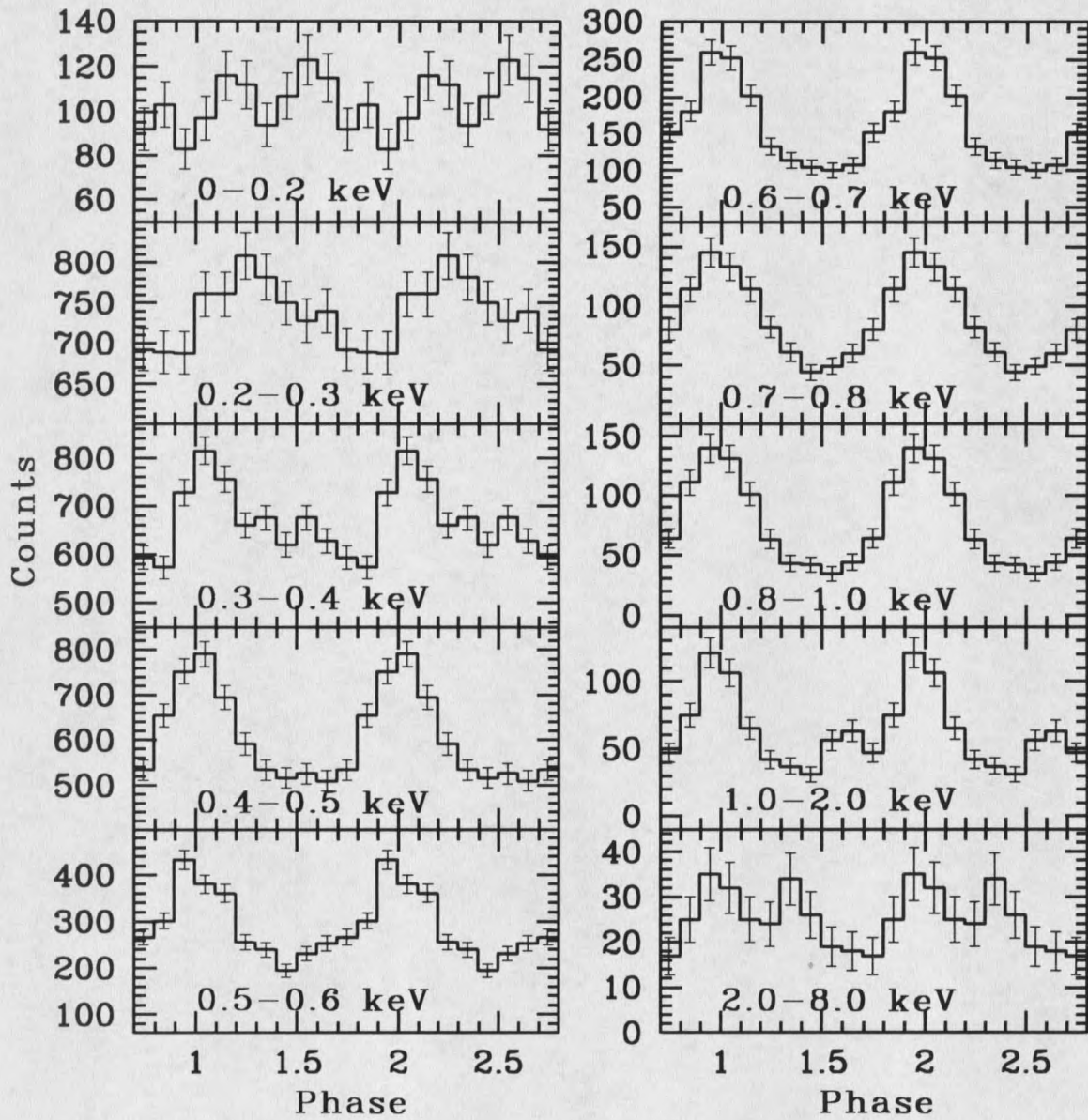


Figure 3.3: Energy resolved light curves of the *Chandra* observation.

higher energy before broadening again. There are two phase shifts present. One is at low energy, at  $\sim 0.3-0.4$  keV of  $\sim 100^\circ$ , while the other is at higher energy but of smaller magnitude,  $\sim 0.8-1.0$  keV of  $\sim 35^\circ$ . The second phase shift is not clearly visible in figure 3.3, but it is clear at higher phase resolution.

Figure 3.4 shows the pulsed fraction as a function of energy. As the energy increases from  $\sim 0.4$  keV to  $\sim 1$  keV, we find the pulsed fraction increasing from  $\sim 15\%$  to  $50\%$ . At higher energy,  $\sim > 2.0$  keV, the pulsed fraction decreases to  $\sim 40\%$ . OF93 found the pulsed fraction to reach  $\sim 80\%$ , but the low number of counts from the *ROSAT* observation makes the value very uncertain. But, our overall trend for the pulsed fraction is consistent with the earlier results of OF93.

### Phase Integrated Spectral Analysis

To carry out spectral analysis of the lower energy part of spectrum for PSR B1055-52, we carried out a combined *ROSAT* and *Chandra* analysis. The *Chandra* data below 0.5 keV was ignored since we found the spectral response to be unreliable. Using *ROSAT* energies above 0.2 keV, we replaced the low energy *Chandra* data set. The data from all phases of the pulsar's rotation were used, thus giving a phase integrated spectrum. Subsequently, we analyzed the phase integrated data spectrum using previous models summarized in table 3.1. Our results are summarized in table 3.2.

A single blackbody model does not fit the spectral data, as the model deviated significantly from the data at nearly all energies. The best fit values of the parameters,

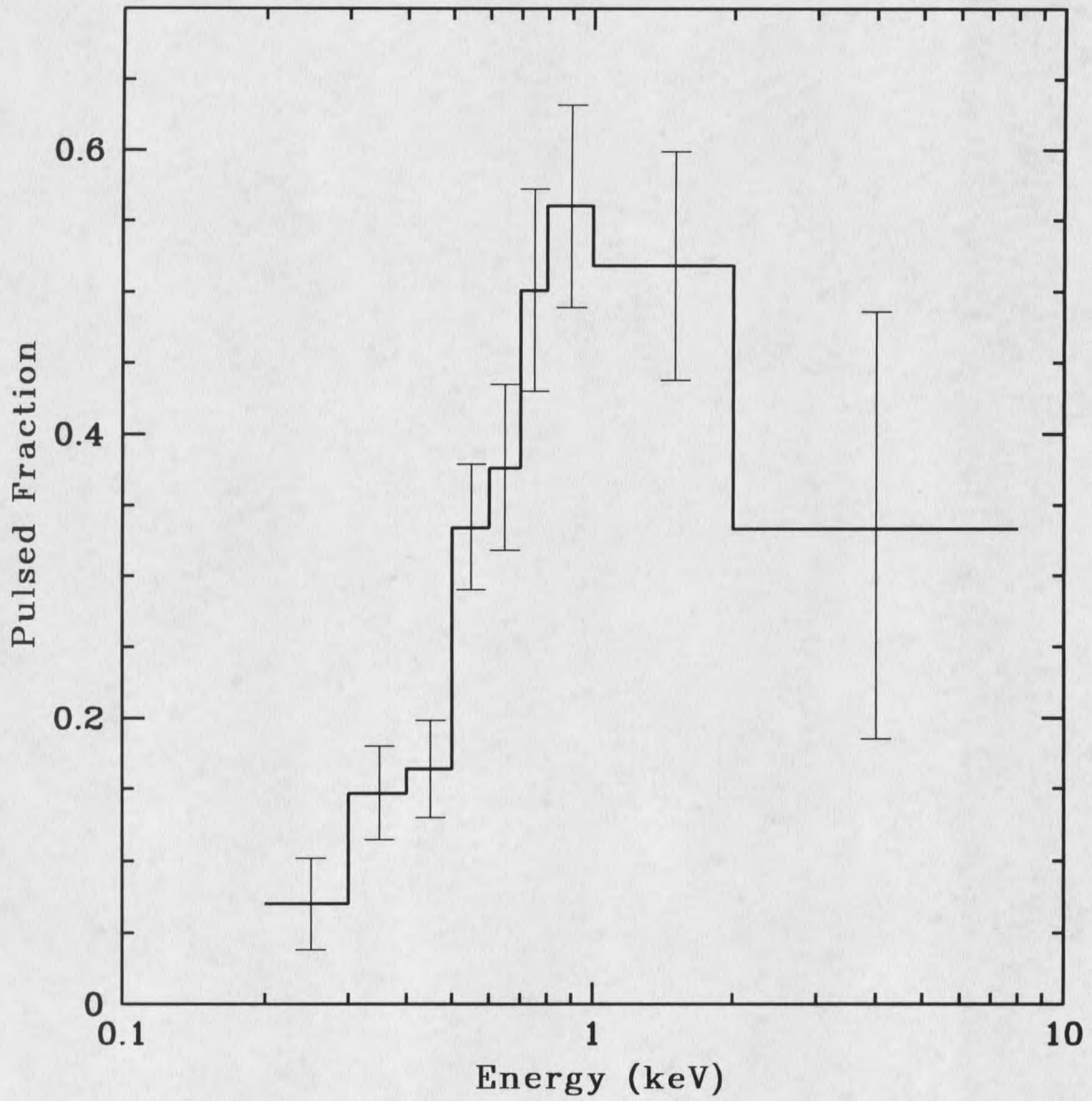


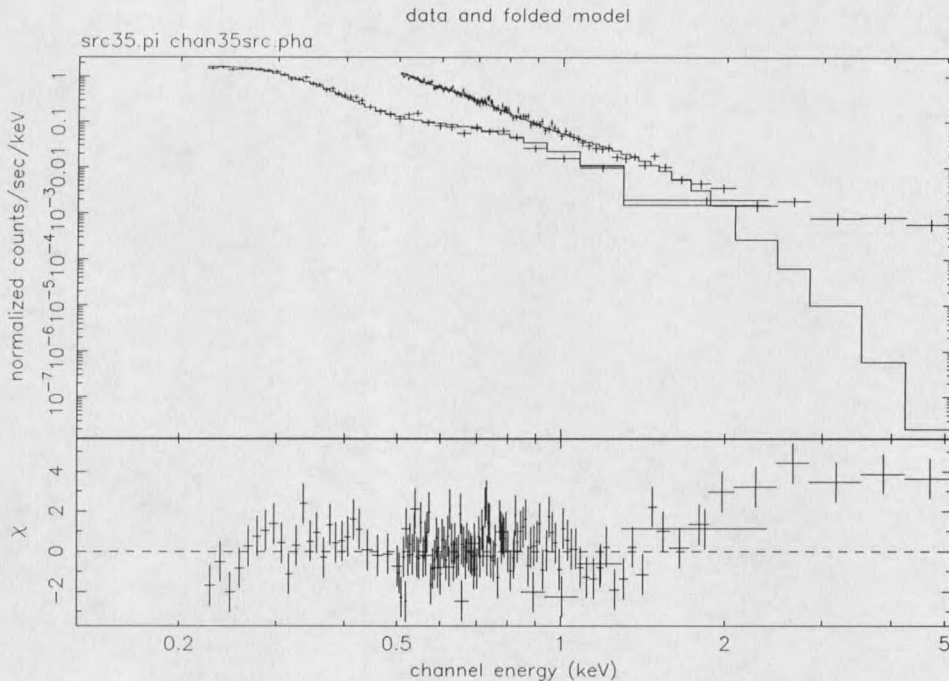
Figure 3.4: Pulsed fraction as a function of energy for the *Chandra* observation

Table 3.2: Summary of X-ray spectral results from combined *ROSAT* and *Chandra* analysis using models from previous work. A single blackbody component is labeled as BB, and a single power-law component is labeled as PO. The hydrogen column density is  $n_H$ . The soft blackbody apparent temperature are labeled  $kT_S$  and radius  $R_S$ . Similarly, the values for the hard blackbody are labeled with  $kT_H$  and  $R_H$ . The power-law index is  $\Gamma$ , and the power-law normalization is  $N_\Gamma$ . The fit statistic is  $\chi^2$ , the degrees of freedom is d.o.f., and  $\chi^2_\nu = \chi^2/\text{d.o.f.}$ .

Parameters	Model			
	BB	PO	BB+BB	BB+PO
$n_H$ ( $10^{20} \text{ cm}^{-2}$ )	34	$6.2 \pm 0.3$	$0.87^{+0.40}_{-0.31}$	$1.4 \pm 0.5$
$kT_S$ (eV)	66	...	$80^{+2}_{-4}$	$77 \pm 4$
$R_S$ (km at 1 kpc)	61	...	$8.5^{+1.9}_{-1.2}$	$9.3^{+2.2}_{-1.6}$
$kT_H$ (keV)	...	...	$0.26^{+0.05}_{-0.04}$	...
$R_H$ (km at 1 kpc)	...	...	$0.16^{+0.10}_{-0.06}$	...
$\Gamma$	...	$5.7 \pm 0.1$	...	$3.3^{+0.4}_{-0.5}$
$N_\Gamma$ ( $\times 10^{-5} \text{ s}^{-1} \text{ cm}^{-2}$ at 1 keV)	...	$11.8^{+0.5}_{-0.4}$	...	$6.5^{+1.6}_{-1.3}$
$\chi^2$	4206.	276.5	243.0	194.3
d.o.f.	139	139	137	137
$\chi^2_\nu$	30.26	1.989	1.774	1.418

as indicated by the large value for  $\chi^2$ , ruled out this model. We found that a single power-law model faired much better, converging to  $\chi^2 = 276.5$  for 139 degrees of freedom; however, we found a large deviation at energies above 1.5 keV suggesting that there was a missing component. Furthermore, the power-law index,  $\Gamma = 5.67$ , lacked an easy physical explanation.

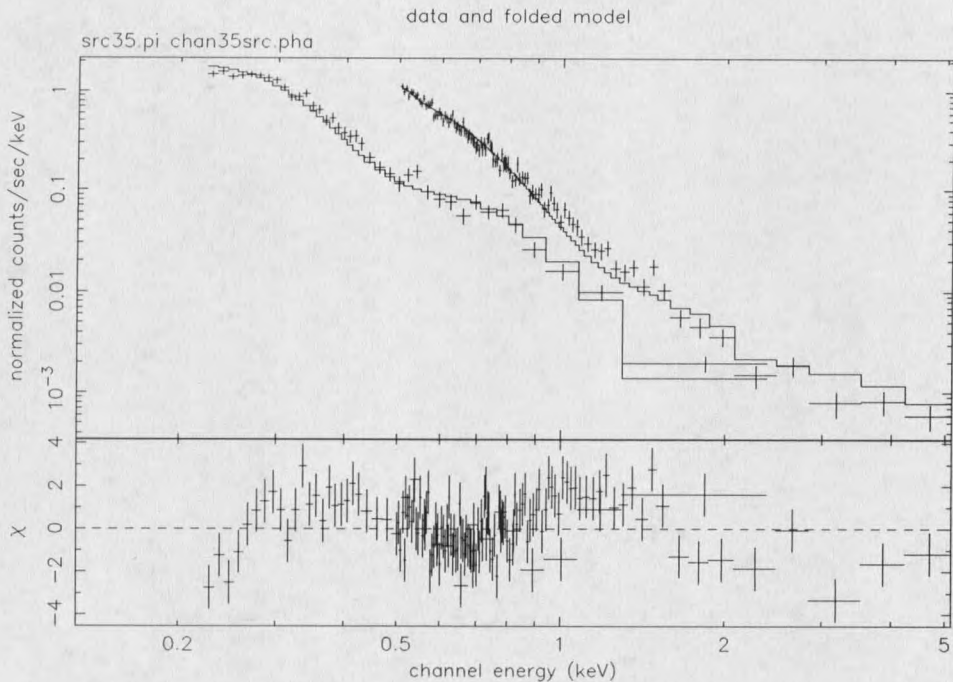
We found two component models to be better, but not great. A two blackbody model converges to  $\chi^2 = 243.0$  for 137 degrees of freedom, shown in figure 3.5. Again we found the residuals to deviate away from the data significantly at the higher energies, suggesting that the two blackbody model lacked a high energy component. A blackbody plus power-law model did better, with a  $\chi^2 = 194.3$ . However, the



20-Jul-2001 18:48

Figure 3.5: Results from PSR B1055-52 combined *ROSAT* and *Chandra* analysis using a two component model, two blackbodies. Notice the deviation of high energy photons in the residual.

power-law index,  $\Gamma = 3.3$ , was inconsistent with the expected index for the pair plasma in the magnetosphere,  $1 < \Gamma < 2$ ; furthermore, we found a deviation of the fit at energies above 3.0 keV. To be consistent with the expected index, we attempted the blackbody plus power-law model with the index fixed at the value determined by W98,  $\Gamma = 1.5$ . Our results for the fixed index are shown in figure 3.6. with the index fixed. The residuals suggested that the model is not a good fit, because of their sinusoidal behavior. Though possible two component models were not exhausted, our results from the light curves suggested a three component model to account for the phase shifts and the energy dependence of the pulse fraction.



20-Jul-2001 19:06

Figure 3.6: PSR B1055-52 combined *ROSAT* and *Chandra* analysis using 2 component, blackbody plus power-law with fixed index,  $\Gamma=1.5$ . The distinctive sinusoidal distribution of the residuals indicate a poor fit.

To make a three component model, we attempted a combination of G96 and W98 two component models. We began constructing our model with the power-law component, trying to extend it to the  $\gamma$ -rays. Our best power-law fit for the optical and the  $\gamma$ -ray observations suggest that the power-law component should have an index  $\Gamma = 1.47$ ; however, the normalization for the best fit predicted a flux in the X-ray band that was higher than the flux for the *Chandra* data above 2.0 keV. Failing to connect the optical and the  $\gamma$ -rays through the X-rays with a single power-law, we concentrated our efforts upon the deviation found in the high,  $>2$  keV, energies for the blackbody plus blackbody and the blackbody plus power-law fits. We assumed

that the missing component was a power-law and checked to see if its index would vary with phase. By calculating the hardness ratio defined as the ratio of the number of photons above and below a reference energy, we found that it did not vary more than its uncertainty for energies above 2 keV in five phase bins. Consequently, we regarded the slope of the power-law component as fixed. We determined the index by fitting the *Chandra* data above 2.0 keV with a single power-law model, finding the best fit for the power-law index to be  $\Gamma = 1.66_{-0.54}^{+0.57}$ . Since our power-law index was consistent with the expected value from the W98 magnetospheric pair plasma model, we chose two blackbodies as the remaining components.

The results of our three component fit are summarized in table 3.3. Since the

Table 3.3: Summary of X-ray spectral results from combined *ROSAT* and *Chandra* analysis using 3 component model.

Parameter	Value	
$n_H$	$1.3_{-0.4}^{+0.5}$	$10^{20} \text{ cm}^{-2}$
$kT_1$	$72. \pm 10.$	eV
$R_1$	$12_{-3}^{+3}$	km at 1 kpc
$kT_2$	$0.14_{-0.03}^{+0.04}$	keV
$R_2$	$0.8_{-0.5}^{+0.8}$	km at 1 kpc
$\Gamma$ (fixed)	1.66	
$N_\Gamma$	$2.0_{-0.5}^{+0.4}$	$10^{-5} \text{ keV}^{-1} \text{ s}^{-1} \text{ cm}^{-2}$ at 1 keV
$\chi^2$	144.08	
d.o.f.	134	
$\chi_\nu^2$	1.08	

power-law index was firmly established, our fits for the model considered it fixed.

The temperatures and the normalizations for our model seemed reasonable, based upon previous results for PSR B1055-52. We chose the distance of 1kpc based upon previous results (e.g. OF93), which was consistent with the expected radius of a neutron star. The fit for this model is in figure 3.7. We noticed that the model fits the data well over all of the energy range. It also showed the two blackbody components crossing at 0.8 keV, giving a natural explanation for the high energy phase shift in the light curves, if we assume that the two components are not exactly in phase with each other; however, we found no obvious explanation for the low energy phase shift with this model. The confidence contours for the fit parameters are shown in figures 3.8 and 3.9.

Another model, a blackbody plus two power-laws was attempted with reasonable fits. The results were suspect because of a photon index for one of the power-law components exceeded  $\Gamma = 2$ , as in the case with the two component blackbody plus a power-law. It failed to explain either of the phase shifts seen in the light curves.

A four component model was tried, three blackbodies and a power-law. The model was found to fit, explaining the 0.4 keV phase shift, but there was no compelling reason to accept the four component fit over the three component fit. An improved *Chandra* response matrix for low energy would be needed to consider such a model.

We considered a few other models, but they resulted in poor fits. Since the physical interpretation for the other models would be in doubt anyway, they aren't included within our results; however, the importance of the magnetic hydrogen atmosphere model results requires mentioning. The results were not rejected because of a poor

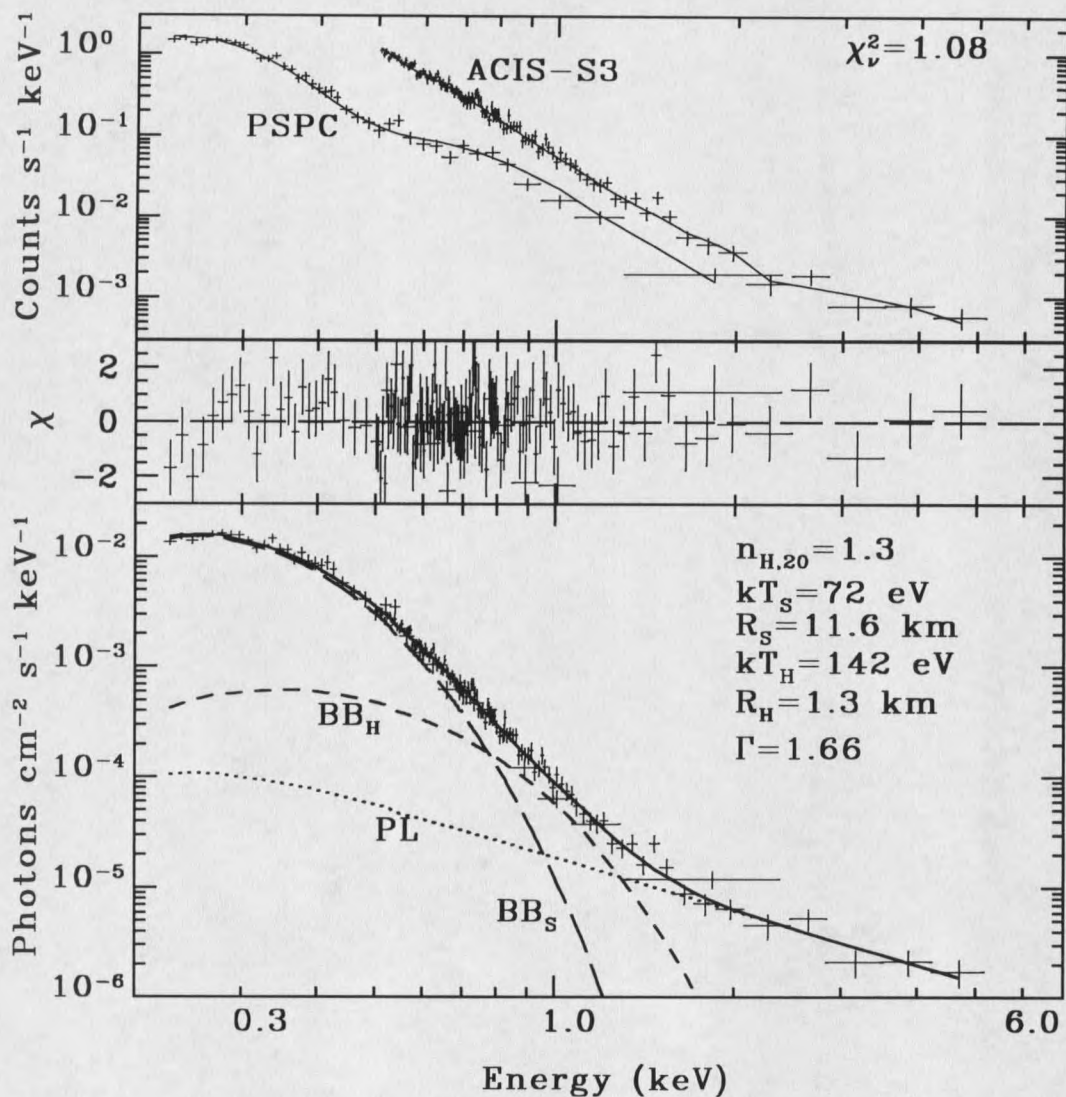


Figure 3.7: Results from our PSR B1055-52 combined *ROSAT* PSPC and *Chandra* ACIS-S3 analysis using three component, two blackbodies plus power-law, model. The top panel shows the raw *ROSAT* (low energy) and *Chandra* (high energy) data sets. The middle panel shows the residual for the fit. The lower panel shows the unfolded spectra with telescope response taken into account. The 3 curves are the soft blackbody component (long dash), the hard blackbody component (dash), and the power-law component (dot). The sum of the three components is the solid line.

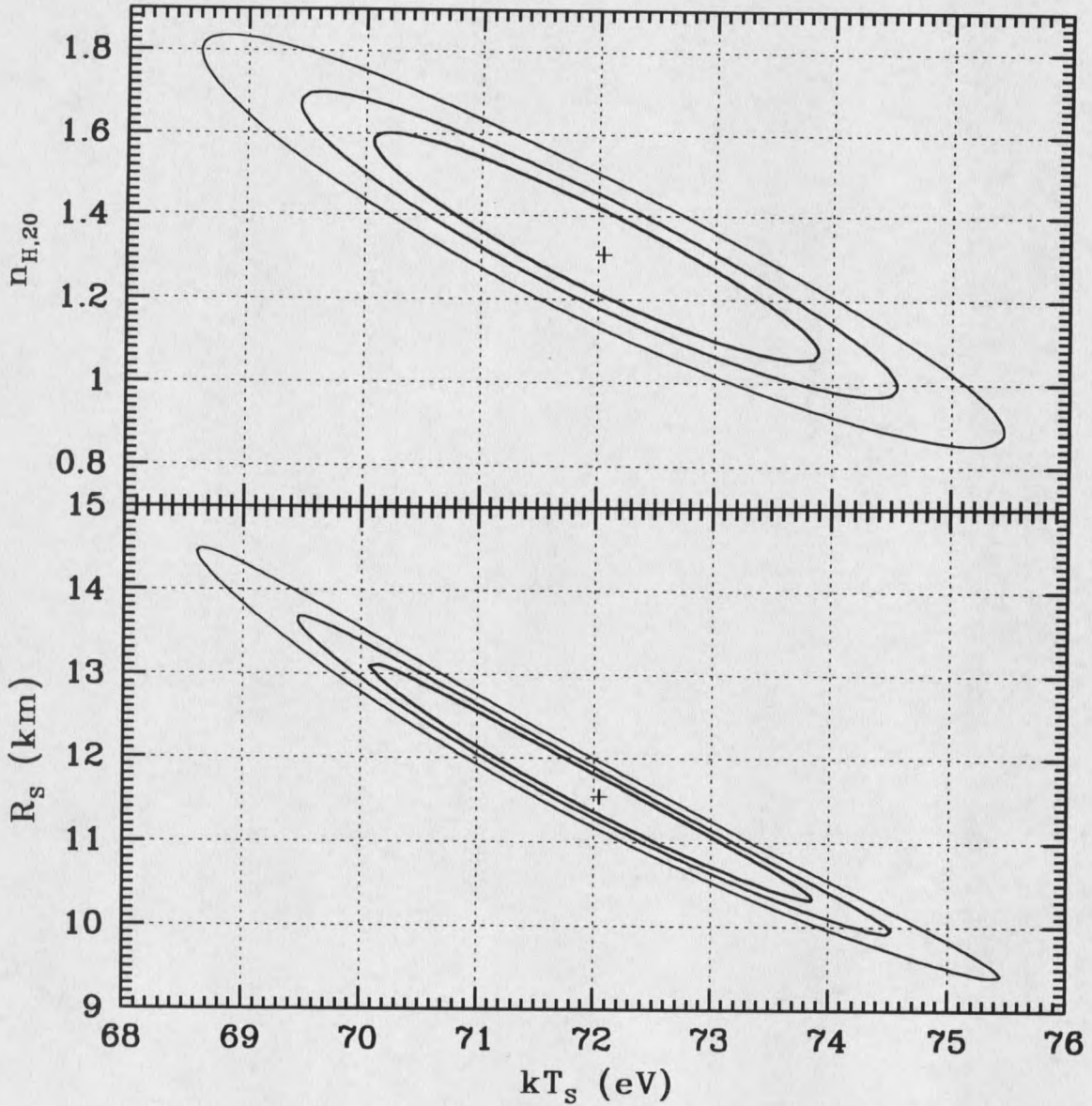


Figure 3.8: Confidence contours for soft blackbody for phase integrated spectrum. The contours are for  $n_{H,20}$  versus  $kT_S$  and  $R_S$  versus  $kT_S$ , where  $n_{H,20} = n_H / 10^{20} \text{ cm}^{-2}$  and  $R_S$  is the soft blackbody radius in km at 1 kpc. The contours are 1 (inner), 1.6 (middle) and 2.6  $\sigma$  (outer) using a 3 parameter fit.

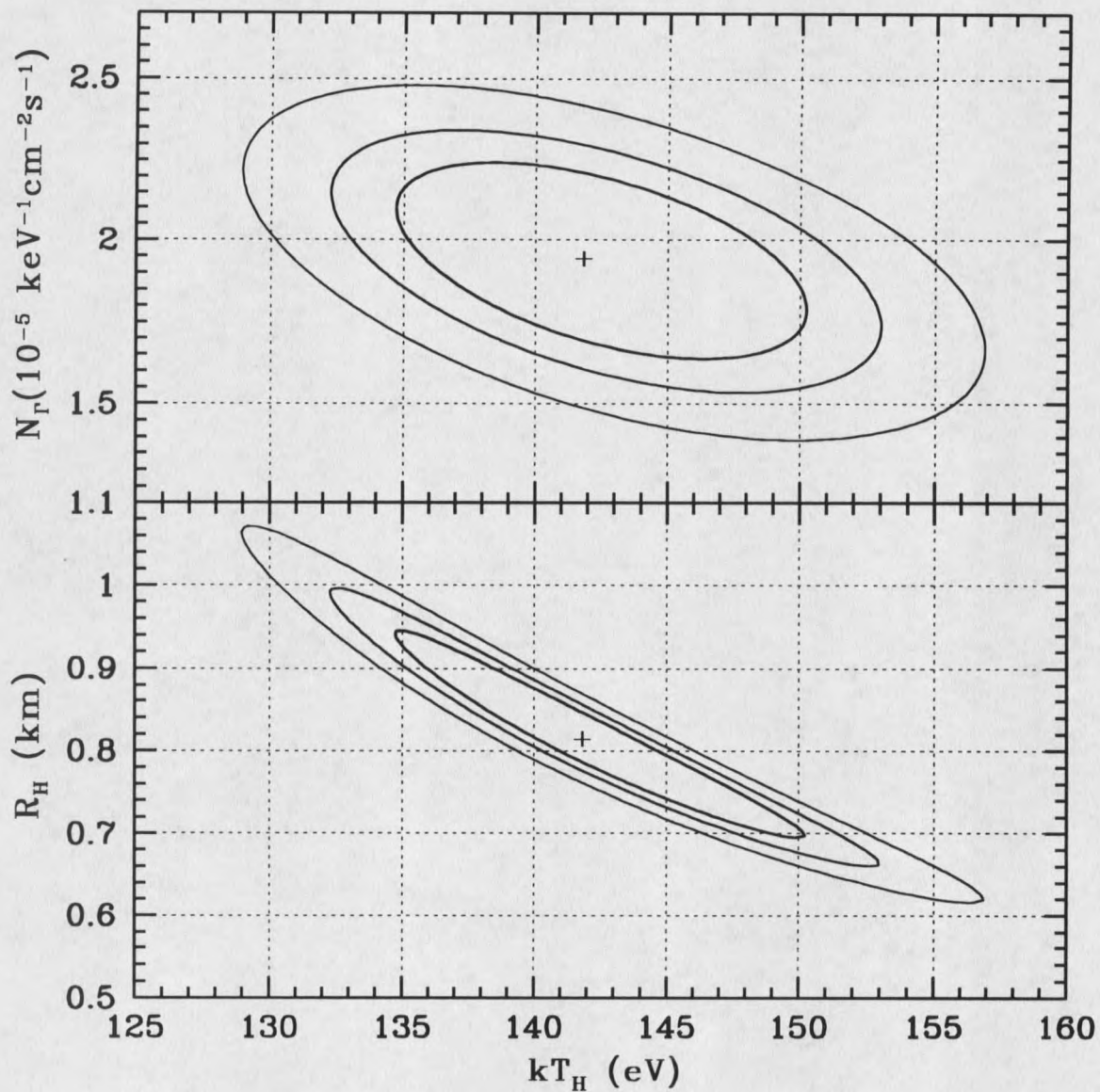


Figure 3.9: Confidence contours for the hard blackbody and power-law normalization for the phase integrated spectrum. The contours are for  $N_\Gamma$  versus  $kT_H$  and  $R_H$  versus  $kT_H$ . Again, the contours are using a 3 parameter fit.

fit but because of the distance of  $\sim 200$  pc that the model predicted. The predicted distance was unacceptable because there would have been a detected large proper motion in the radio observations. No such proper motion has been reported, so the short distance is rejected.

### Phase Resolved Spectroscopy

We attempted phase resolved spectroscopy to see the variation of spectral parameters with phase. For the phase resolved spectroscopy, the *ROSAT* data set was rejected because of its uncertain phase, so only *Chandra* data set above 0.5 keV was considered for the fitting. The observation was divided into five phase bins, concluding that five were optimal for error considerations. After dividing into phase bins the models were again tested for each phase, noting the fits and the differences between the varied model parameters. Only our three component model, two blackbodies plus a power-law, was used for phase resolved spectroscopy.

All of the model parameters could be varied from their phase integrated results with the exception of the hydrogen column density,  $n_H$ . Since  $n_H$  is a measurement of absorption between the observer and the target, we considered it to be independent of time. It might vary with time, but such variations should not be on the time scale of the observation, 30 ks, nor the period of the pulsar,  $\sim 200$  ms. The variations of the interstellar medium would be irrelevant in this case. Subsequently, we regarded the phase integrated value of  $n_H$  as fixed.

Tables 3.4 and 3.5 shows the results for the phase resolved spectroscopy for fixing

a different set of parameters. In the first case, the soft blackbody normalization and the hard blackbody temperature were fixed. In the second case the soft blackbody temperature and hard blackbody normalization were fixed. Both cases left the model to be fit with a three parameter fit. We fixed the parameters to improve fitting accuracy with a low number of counts. The two cases were developed to avoid the prejudice imposed by fixing the parameters.

Table 3.4: Summary of X-ray spectral results from phase resolved *Chandra* analysis using 3 component model, case 1. The fixed parameters are  $n_H=1.3 \times 10^{20} \text{ cm}^{-2}$ ,  $R_s=11.6 \text{ km}$  at 1 kpc,  $kT_H=0.14 \text{ keV}$ , and  $\Gamma=1.66$ .

Parameters	Phase				
	-0.1 - 0.1	0.1 - 0.3	0.3 - 0.5	0.5 - 0.7	0.7 - 0.9
$kT_s$	$73_{-1}^{+1}$	$73_{-1}^{+1}$	$71_{-1}^{+1}$	$71_{-1}^{+1}$	$72_{-1}^{+1}$
$R_H$	$1.3_{-0.1}^{+0.1}$	$0.9_{-0.1}^{+0.1}$	$0.2_{-0.2}^{+0.2}$	$0.5_{-0.2}^{+0.2}$	$0.9_{-0.1}^{+0.1}$
$N_\Gamma$	$3.5_{-1.4}^{+0.5}$	$1.0_{-1.0}^{+0.5}$	$2.0_{-0.6}^{+0.6}$	$2.4_{-1.0}^{+0.4}$	$2.2_{-0.8}^{+0.8}$
$\chi^2$	34.38	33.70	24.51	25.96	36.69
d.o.f.	48	31	20	22	34
$\chi_\nu^2$	0.72	1.09	1.23	1.18	1.08

Table 3.5: Summary of X-ray spectral results from phase resolved *Chandra* analysis using 3 component model, case 2. The fixed parameters are  $n_H=1.3 \times 10^{20} \text{ cm}^{-2}$ ,  $kT_s=72 \text{ eV}$ ,  $R_H=0.82 \text{ km}$  at 1 kpc, and  $\Gamma=1.66$ .

Parameters	Phase				
	-0.1 - 0.1	0.1 - 0.3	0.3 - 0.5	0.5 - 0.7	0.7 - 0.9
$R_s$	$13.2_{-0.6}^{+0.6}$	$11.9_{-0.5}^{+0.5}$	$10.6_{-0.6}^{+0.6}$	$10.7_{-0.7}^{+0.5}$	$11.8_{-0.5}^{+0.4}$
$kT_H$	$163_{-5}^{+3}$	$143_{-4}^{+5}$	$94_{-94}^{+21}$	$93_{-93}^{+22}$	$146_{-5}^{+4}$
$N_\Gamma$	$3.0_{-1.7}^{+0.7}$	$0.6_{-0.6}^{+0.8}$	$2.1_{-0.6}^{+0.2}$	$2.0_{-0.5}^{+0.5}$	$2.2_{-1.0}^{+0.7}$
$\chi^2$	42.64	33.19	24.46	24.44	37.62
d.o.f.	48	31	20	22	34
$\chi_\nu^2$	0.89	1.07	1.22	1.22	1.11

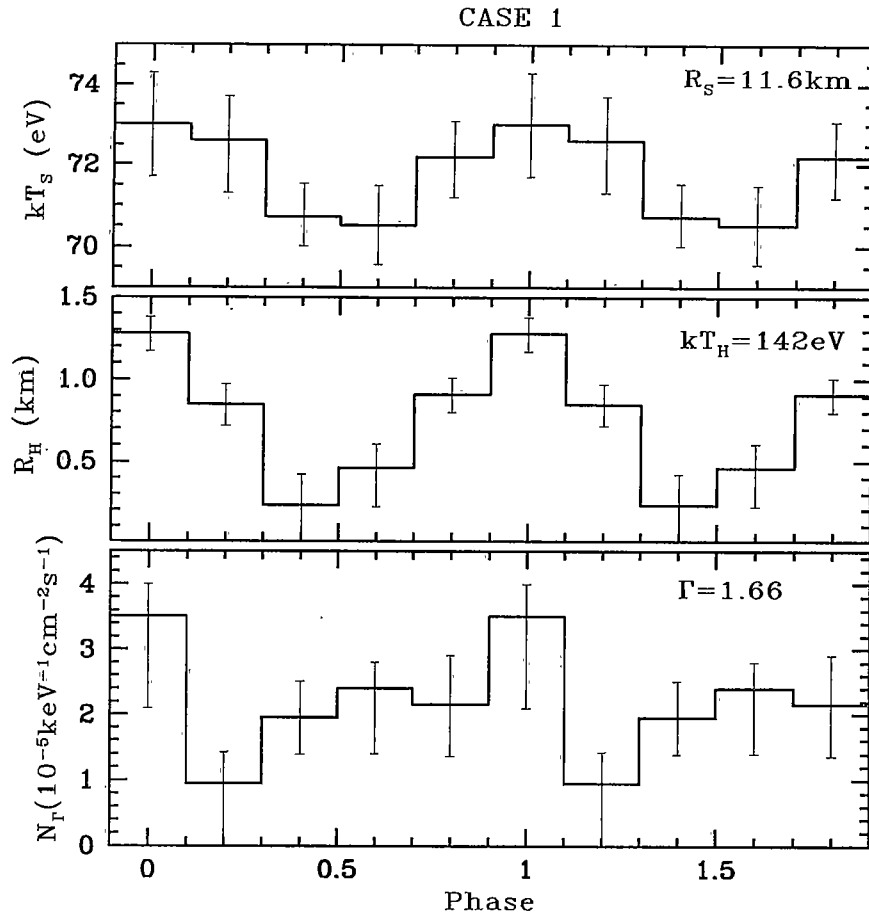


Figure 3.10: Phase resolved spectroscopy results case 1. The fixed parameters are labeled within the panels. The hydrogen column density,  $n_H$  was fixed at a value of  $1.3 \times 10^{20} \text{ cm}^{-2}$ .

Figure 3.10 shows the first case where  $R_S$  and  $kT_H$  were held fixed. The variability of the free parameters are shown as a function of phase. The variation of the hard blackbody radius was found to be strong, while the soft blackbody temperature did not vary much more than its error. Figure 3.11 shows the second case where we held  $kT_S$  and  $R_H$  fixed. Again, we found that the soft blackbody component, in this case the radius, did not vary to a large extent. However, the hard blackbody temperature

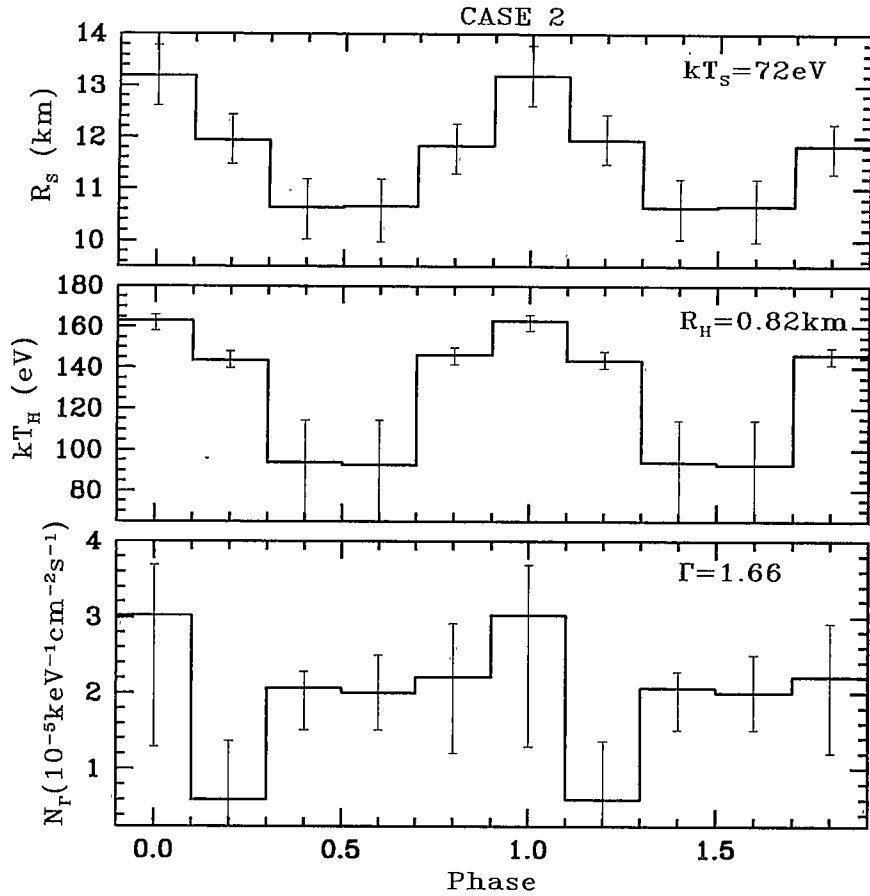


Figure 3.11: Phase resolved spectroscopy results case 2. Again, the hydrogen column density,  $n_H$  was fixed at a value of  $1.3 \times 10^{20} \text{ cm}^{-2}$ .

showed significant variation. In both cases the power-law normalization,  $N_\Gamma$ , showed similar variation with phase.

The bolometric flux of the individual components was calculated. In the case for the power-law component, the flux from 0.1 to 10 keV was found. Since the power-law index was fixed, then the flux behaves just like the power-law normalization, which has the units of flux at 1 keV. To conveniently construct the flux, we froze the parameters for the phase resolved spectra to their best fit values. Then, one component was fit to

the spectra. For example, to determine the soft blackbody bolometric flux in phase 0.7-0.9, first the spectral components were fixed at their best fit value. We then fit the soft blackbody temperature and normalization to the spectra. The final fit values were used to compute the flux for the soft blackbody at phase 0.7-0.9. The error for the flux was computed using a confidence contour for the component. We chose the contour as  $\delta\chi^2 = 1$ . By calculating the flux at points along the contour, the extremes of the flux were established as our upper and lower limits. The unabsorbed fluxes are presented in figures 3.12 and 3.13 as a function of phase.

For case 1, we found that the soft blackbody flux did not vary more than its uncertainty. The soft blackbody temperature was seen to have variability to nearly within its uncertainty. We concluded from Case 1 that all of the variability was due to the hard blackbody flux and the power-law. We considered this a contradiction because it did not explain variability of the light curves at the lower energy range.

In case 2, the soft blackbody flux was found to vary, but it was in phase with the hard blackbody flux. Though the phase resolution of the phase resolved spectroscopy was insufficient to view the high energy phase shift, at  $\sim 0.8$  keV, we found no indication of variation in the hard blackbody model to explain the large phase shift at low energy.

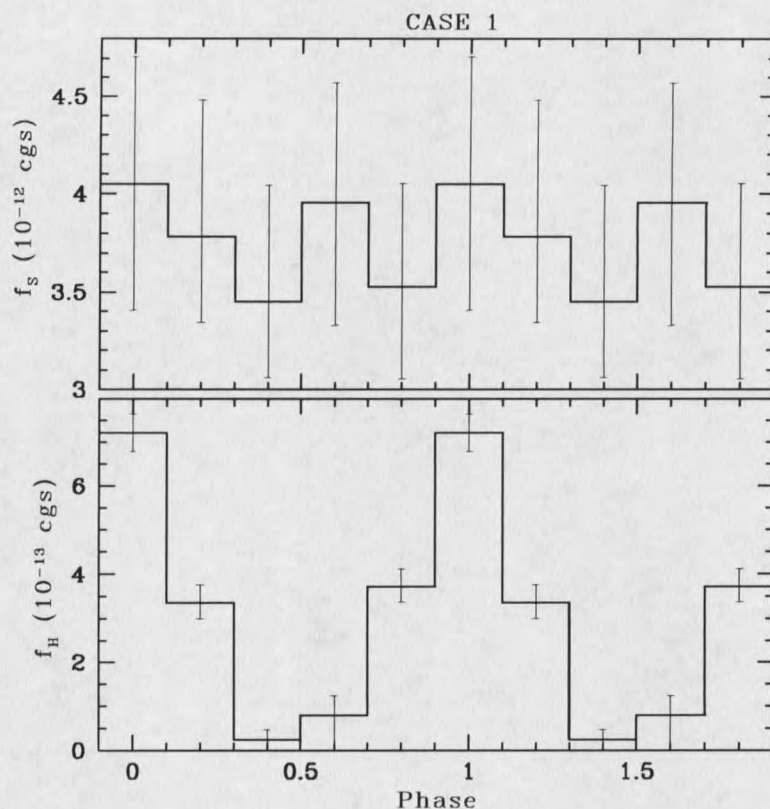


Figure 3.12: Phase variation of blackbody bolometric fluxes (Case I). For the blackbody components the flux was computed by fixing the other parameters to their best fit values for each phase. The errors in the flux were estimated from a  $\chi^2_{min} + 1$  contour for the model component. The cgs units are  $\text{ergs s}^{-2} \text{cm}^{-2}$ .

### Discussion

Earlier results suffered from poor counting statistics from the *ROSAT* and *ASCA* observations. Our findings from the combined *ROSAT* and *Chandra* data analysis show that two component models will not fit the data accurately. Neither the G96 two blackbody model, nor the W98 blackbody plus power-law model would fit the combined *ROSAT* and *Chandra* data. Using the G98 model, there is a significant deviation at high energy, while using the W98 model shows oscillatory behavior in

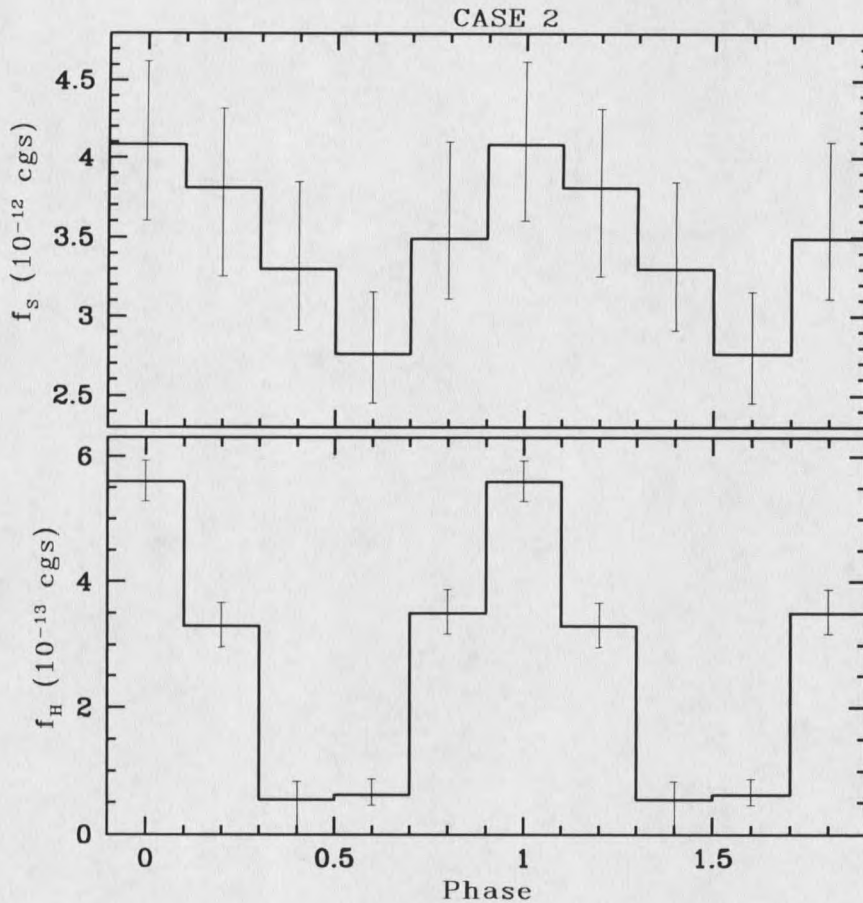


Figure 3.13: Phase variation of blackbody bolometric fluxes (Case II). See caption for figure 3.12 for details.

the residual. Furthermore, if we allowed the power-law index to vary, the best fit for the index is  $\Gamma \sim 3$ , which is inconsistent with non-thermal radiation expected from a magnetospheric pair plasma.

Our results for the phase integrated spectra for the combined *ROSAT* and *Chandra* observation require a three component model. First, the model requires a soft blackbody component, which we interpreted as thermal radiation from the neutron star surface. Secondly, a hard blackbody component is needed, which we considered

as a hot spot associated with one of the magnetic poles. Lastly, a power-law component is needed to account for the highest energy photons detected. The index,  $\Gamma=1.66$ , is consistent with a pair plasma for the magnetosphere.

Our temporal results, figures 3.3 and 3.4, show interesting trends. First, the pulsed fraction indicates a slow increase from 0.2 to 0.5 keV, to a value of  $\sim 15\%$ . Furthermore, the phase changes at approximately 0.4 keV with an angle of  $\sim 100^\circ$ . Above 0.5 keV, we found a sharp increase of pulsed fraction to about 50% at 0.8 keV, corresponding to the shift between the hard and soft blackbody components, see figure 3.7. We interpret the increasing pulsed fraction as the hard component becoming more dominant as the energy increases. It follows that the soft blackbody component could be interpreted as the overall neutron star surface with a temperature distribution, while the hard blackbody component represents a hot spot. The large pulsed fraction at 0.8 keV suggests, by our geometric models, that magnetic axes and the rotation axes are separated by a large angle. The decrease in pulsed fraction to about 40% above 2.0 keV, where the power-law component dominates, would be inconsistent with a higher pulsed fraction expected for the magnetospheric non-thermal radiation (Tsuruta, 1998), but the measured smaller pulsed fraction is due to a lack of counts at these higher energies.

The phase shift near 0.4 keV, with the lower energy peak lagging higher energy peak and the radio peak by  $\sim 100^\circ$ , has two possible explanations, an off-center magnetic dipole configuration (Halpern and Ruderman 1993), and multipole magnetic field structure (Page and Sarmiento 1996).

An off-center dipole configuration gives an easy explanation for the phase shift between the softer and harder components. If the dipole is off center toward one side of the star, the soft thermal component will tend to be hotter on one side than the other. Using the result of Greenstein and Hartke (1983) for the temperature modulation,  $T(\theta) = (\cos^2\theta + \chi_o \sin^2\theta)^{1/4} T_o$ , with  $T_o$  being the surface temperature at the magnetic pole,  $\chi_o$  being the ratio of parallel and perpendicular components of thermal conductivity, and  $\theta$  being the angle between the magnetic field and the surface normal. Such a configuration would naturally explain the  $\sim 100^\circ$  phase shift seen at 0.4 keV. This had been adapted to explain, in part, the phase shift for the Geminga pulsar (Halpern and Ruderman 1993).

A multipole magnetic field can be used to model complex temperature distributions upon neutron star surfaces. If a neutron star's magnetic field configuration is not a simple dipole, then the multipole field can be adapted to show many different distributions of temperature. The multipole field has up to five quadrupole field components with various strengths. Page and Sarmiento (1996) fit the multipole field to several pulsars using *ROSAT* data, including PSR B1055-52. The results showed that the phase shifts due to the temperature distribution of the multipole field case could be easily explained. However, the pulsed fraction required additional beaming to explain.

Our radius for PSR 1055-52 assumes an optimum distance of about 1 kpc. This could have easily been done by first assuming a radius for the neutron star and then computing the distance. For a stiff EOS, the neutron star is at its maximum radius.

Assuming a 1.4 solar mass ( $M_{\odot}$ ) and a stiff EOS, the radius will be  $R=15\text{km}$ , and the distance  $d=1.3_{-3}^{+4}$  kpc. For a soft EOS with the same mass,  $R=7.7\text{km}$ , and a distance of  $d=0.7\pm 0.2$  pc. All are within the range of the distance established by other means (OF93).

## CHAPTER 4

## CHANDRA OBSERVATIONS OF SGR 1900+14

IntroductionMagnetars

Magnetars are a subclass of neutron stars with extremely high,  $\sim > 10^{14}$  Gauss, magnetic fields. The huge magnetic field is expected to produce excessive heating in the magnetar due to the magnetic field decay, thereby giving it an extreme surface temperature. The ultra-high magnetic field also increases the conductivity enormously, resulting in a photon luminosity of  $10^{35}$  erg s<sup>-1</sup> (Kulkarni et al., 2000).

There are two types of sources that are thought to be magnetars, though some still disagree with this assessment (e.g. DeDeo, Psaltis & Narayan, 2001). They are anomalous X-ray pulsars (AXP) and soft gamma-ray repeaters (SGR). Kulkarni et al. (2000) have suggested that the only difference between the two is the magnetic field topology, where SGR derive their characteristic bursts from a tangled field rearranging in a catastrophic reconnection. Duncan (2001) pointed out that both AXP and SGR are associated with smaller SNR. Perna et al. (2001) has also showed that both AXP

and SGR data fit a magnetar model with consistent values for radius of a neutron star, with the exception of AXP RXS J1708-40.

Regardless, whether both AXP and SGR are magnetars, they are expected to become X-ray dark after a relatively short period. Assuming that a magnetar does not have an envelope of light elements, such as hydrogen or helium, they are expected to become X-ray dark within  $10^6$  years; however, if such an envelope exists then their observable lifetime will be as short as  $10^4$  years. Once the liquid interior of the magnetar cools sufficiently, it will halt ambipolar heating (Duncan 2001).

#### Soft Gamma-ray Repeaters(SGR)

Soft gamma ray repeaters (SGR) are  $\gamma$ -ray sources that have a spectrum of energies less than 100 keV. There are short and unpredictable outbursts of activity which last for days, or perhaps months, with long periods, years, of quiescence. There are four or five such sources detected, SGRs 1806-20, 1900+14, 0525-66, 1627-41, and possibly SGR 1801-23 (Duncan, 2001). All but SGR 1801-23 have had Super-Eddington luminosity,  $L > L_{Eddington}$ , bursts. SGRs 1900+14 and 0525-66 have had long duration giant flare events that are three orders of magnitude more energetic than the regular bursts (Hurley 1999). Flares have huge energies associated with them,  $\sim 10^{44}$  ergs, while intermediate scale events are approximately two orders of magnitude less energetic. Bursts are the least energetic at  $\sim 10^{41}$  ergs, but there seems to be a continuum of energies associated with these events (Kouveliotou, 2001).

Thompson and Duncan (1998) have pointed out that the nature of SGR is still

uncertain, but the magnetar model seems to be the most promising. Furthermore, they indicate that there is good evidence that all SGRs are associated with supernova remnants, and the large proper motion of SGR 0525-66 is inconsistent with a neutron star in a tight binary orbit. They also point out that the quiescent X-ray Luminosity of the plerion surrounding SGR 1806-20 cannot be powered by accretion. Furthermore, the X-ray flux from SGR in outburst is a million to a billion times the X-ray flux in quiescence (Thompson & Duncan, 1996).

#### Previous Outbursts of SGR 1900+14

SGR 1900+14 was discovered in 1979 when it burst 3 times (Mazets et al., 1979). In the following years, it was the least active of the SGRs, having only a series of bursts in 1992 (Kouveliotou et al., 1993), until May of 1998, when it had a large outburst. In the following August, SGR 1900+14 had a giant flare, the largest such event.

Prior to the 1998 events, the location of SGR 1900+14 was not precisely known. Data from the solar polar exploration satellite, *Ulysses*, the burst and transient source experiment on CGRO, BATSE, and the  $\gamma$ -ray burst detector, KONUS, on the Wind satellite gave its location to within a 1.6 arc minute circle near the SNR G42.8+0.6. The association between these two objects gives the SGR a transverse velocity 480-5500 km s<sup>-1</sup>. The estimated velocities of other SGR are also high, so this is not unusual (Hurley et al., 1998a).

In 1998 ASCA was used to determine the location of the quiescent X-ray source

a month before the May outburst. The *ASCA* detection gave further evidence to the location of SGR 1900+14. The period was found to be  $P=5.1589715\pm 0.0000008$  s. The best fit for the spectral data for the source was a power-law with photon index of  $2.25\pm 0.04$  and hydrogen column density  $n_{H,22} \equiv n_H/(10^{22} \text{ cm}^{-2})=2.16\pm 0.07$ .

Several observations both prior to and after the 1998 outburst have established periods for SGR 1900+14. There is an increasing trend of the period over the times before and after the outburst; however, Woods et al. (1999) noticed a jump in the linear extrapolations of the periods immediately before and after the August outburst of  $\Delta P=0.57$  ms. They interpret it as a breaking glitch. Their extrapolated period derivative was  $6.13\times 10^{-11} \text{ s s}^{-1}$  before the August 1998 event, and  $6.07\times 10^{-11} \text{ s s}^{-1}$  after the event. Furthermore, they used *RXTE* to determine the period derivative of SGR 1900+14. Their period derivatives were found to be  $8.2\times 10^{-11} \text{ s s}^{-1}$  before the flare, and  $5.93\times 10^{-11} \text{ s s}^{-1}$  after the flare. In either case, the changes of the period derivative suggest that the spin-down rate of SGR 1900+14 is not steady.

#### April 2001 Event

Since 1998, SGR 1900+14 had been in quiescence. Then on 18 April 2001 at 7:55:12 UT, it became active again with a large flaring event detected by the Italian-Dutch satellite *BeppoSAX* using the  $\gamma$ -ray burst monitor, with a flux of 15400 counts per second for a duration of approximately 40 seconds (Frontera 2001). Data from *Ulysses* confirmed the giant  $\gamma$ -ray flare (Hurley 2001). The Schmidt telescope at Tautenburg was used in the I-band and did not find an optical point source down to

magnitude  $I = 21$ , within 18 hours of the flare (Klose 2001).

Subsequently, many instruments around the world began multi-frequency observations in the aftermath of the burst. *BeppoSAX* initiated a followup observation in the  $\gamma$ -ray band within 15 hours of the flare (Feroci 2001). Millimeter observations were done at the IRAM Plateau de Bure Interferometer on April 24, though no source was detected (Bremer 2001). Furthermore, the very large array (*VLA*) radio observation failed to detect the source (Fox et al. 2001). Other radio observations gave similar results (e.g. Kouveliotou et al. 2001).

In the X-ray, both *RXTE* and *Chandra* observed SGR 1900+14 twice within a week of the outburst. The second observations, on 30 April, overlapped. The two *Chandra* observations, 22 April and 30 April, were part of the Director's Discretionary Time (DDT) allocation, with lengths of 20.8 ks and 18.9 ks, respectively and were made available to the public domain almost immediately. The two *RXTE* observations began on 21 April and 30 April and lasted 15.2 and 15.6 ks respectively.

The *Chandra* observations were done in Continuous Clocking (CC) mode to provide 2.8 ms timing resolution. The excellent timing resolution of *RXTE* gave a good confirmation of the pulsation period detected from the source. The results which follow are from the two CC mode *Chandra* observations.

## Our Results

We investigated the timing information of the two *Chandra* observations, attempting to see differences between the two observations. Our investigation of the spectral information, which focused upon seeing if there was a favored spectral fit clearly showed a blackbody component. Furthermore, with our phase resolved analysis, we hoped to uncover any information regarding the phase behavior of any of the spectral components, or a variation between the two observations.

### Our Timing Results

We established the period of SGR 1900+14 by using the  $Z_1^2$  (Rayleigh) statistic. Each observation was corrected for telescope dither and the times were corrected to the solar system barycenter. We present the results of the two observations in figure 4.1. The  $Z_1^2$  is shown versus frequency compared to the frequency when  $Z_1^2$  is maximum for the first observation. For the first observation we found that  $f_{0,1} = 0.1933143^{+1.0e-06}_{-1.3e-06}$  Hz, corresponding to a period of  $P_{0,1} = 5.172923^{+3.4e-5}_{-2.7e-5}$  s. In the second observation we found  $f_{0,2} = 0.1933130^{+1.7e-06}_{-2.0e-06}$  Hz, corresponding to a period of  $P_{0,2} = 5.172958^{+4.3e-5}_{-4.6e-5}$  s. We computed the errors by noting that  $Z_1^2$  is equivalent to  $\chi^2$ , so for a  $1\sigma$  error,  $\delta Z_1^2 \sim 1$ .

Our periods for the two observations, combined with periods reported for the *BeppoSAX* observation (Feroci et al, 2001), and the two *RXTE* observations (Fox et al, 2001), show an increasing trend. A linear regression fit of the periods gives a period

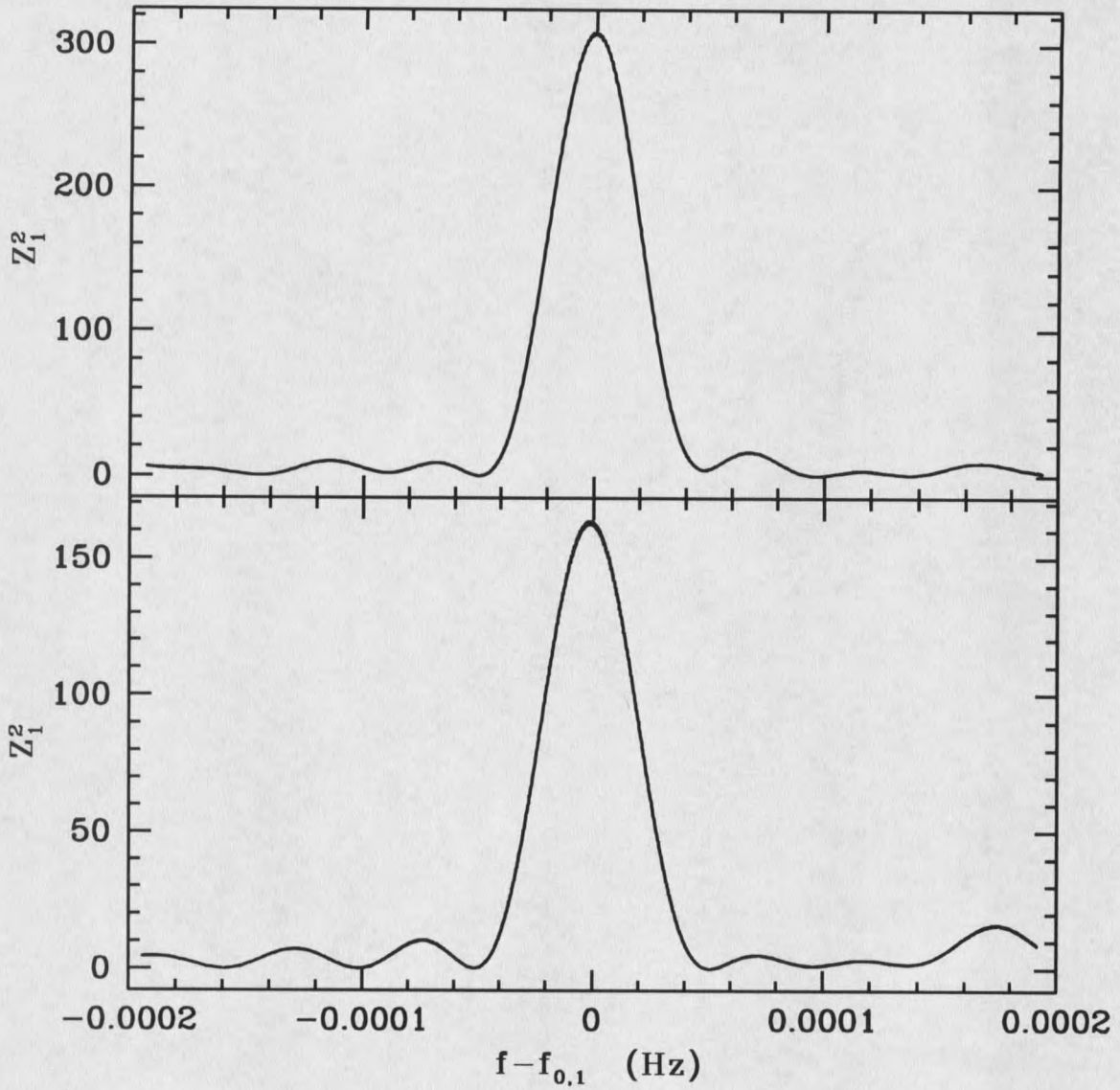


Figure 4.1: Comparison between first (top panel) and second (bottom panel) observation's  $Z_1^2$  statistic. Both are compared to the best fit frequency for observation 1,  $f_{0,1} = 0.1933143_{-1.3e-06}^{+1.0e-06}$  Hz. Note the slight shift for the second observation.

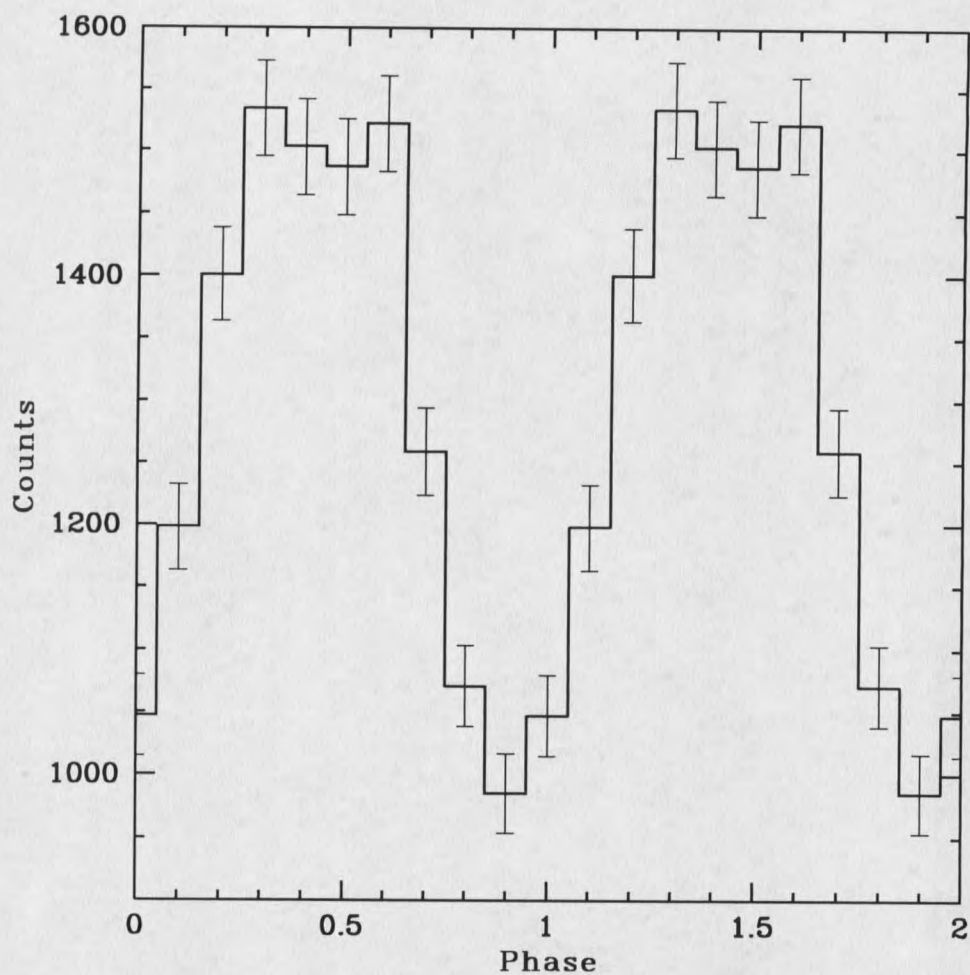


Figure 4.2: Light curve for the first *Chandra* observation.

derivative,  $\dot{P} = 2.23 \pm 0.66 \times 10^{-11} \text{ s s}^{-1}$ . It is interesting to note that an extrapolation of the period derivatives from Woods et al. (1999) show a discrepancy of over 7 ms if extrapolated to the times of the 2001 observations. Our period derivative, however, is still well within the range of period derivatives seen in previous observations (e.g. Woods, et al. 1999).

Our timing analysis of both observations yielded energy resolved light curves. Figures 4.2 and 4.3 present our light curves for the entire *Chandra* range, 0.5-10.0

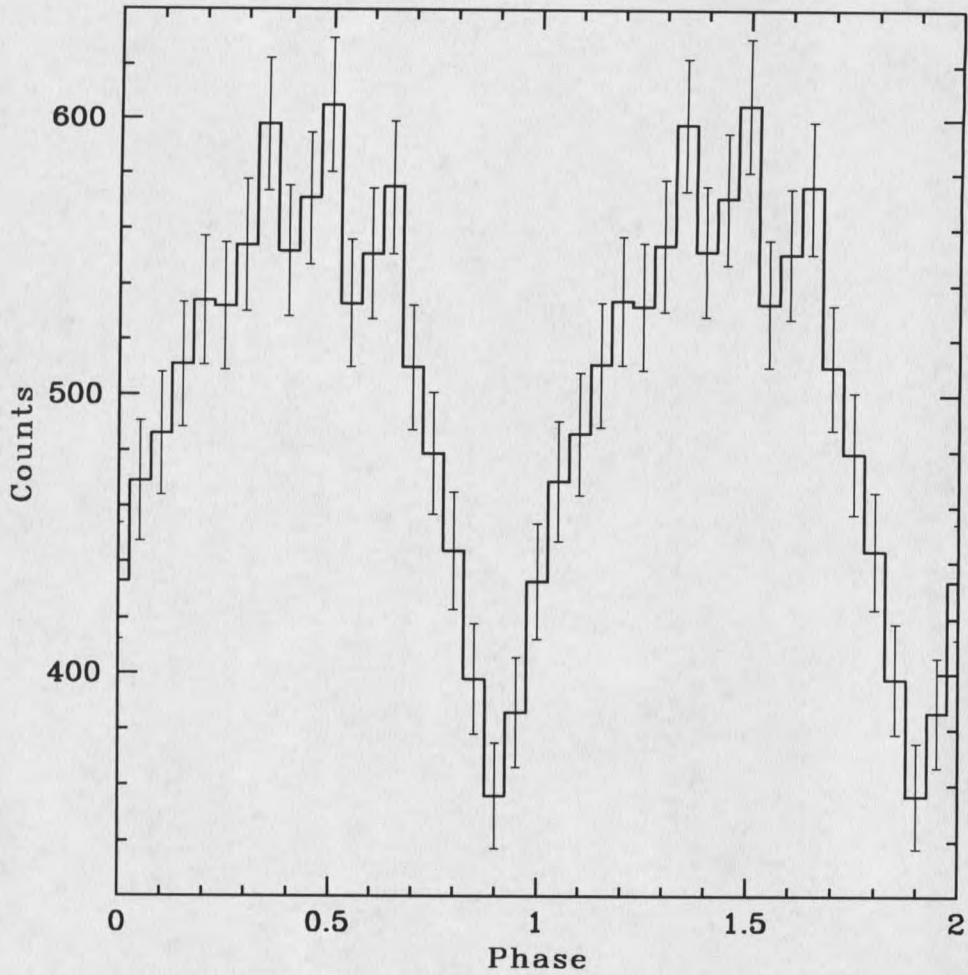


Figure 4.3: Light curve for the second *Chandra* observation.

keV, of the two data sets. Figures 4.4 and 4.5 show our light curves for the two observations as a function of energy. The light curves for the first and the second observation differ little except for count rate. Using the statistic  $S$  given by:

$$S = \sum_i^I \frac{(Nm_i - Mn_i)^2}{N^2m_i + M^2n_i} \quad (4.1)$$

where  $N = \sum n_i$  and  $M = \sum m_i$ , we quantified the difference between two light curves. It

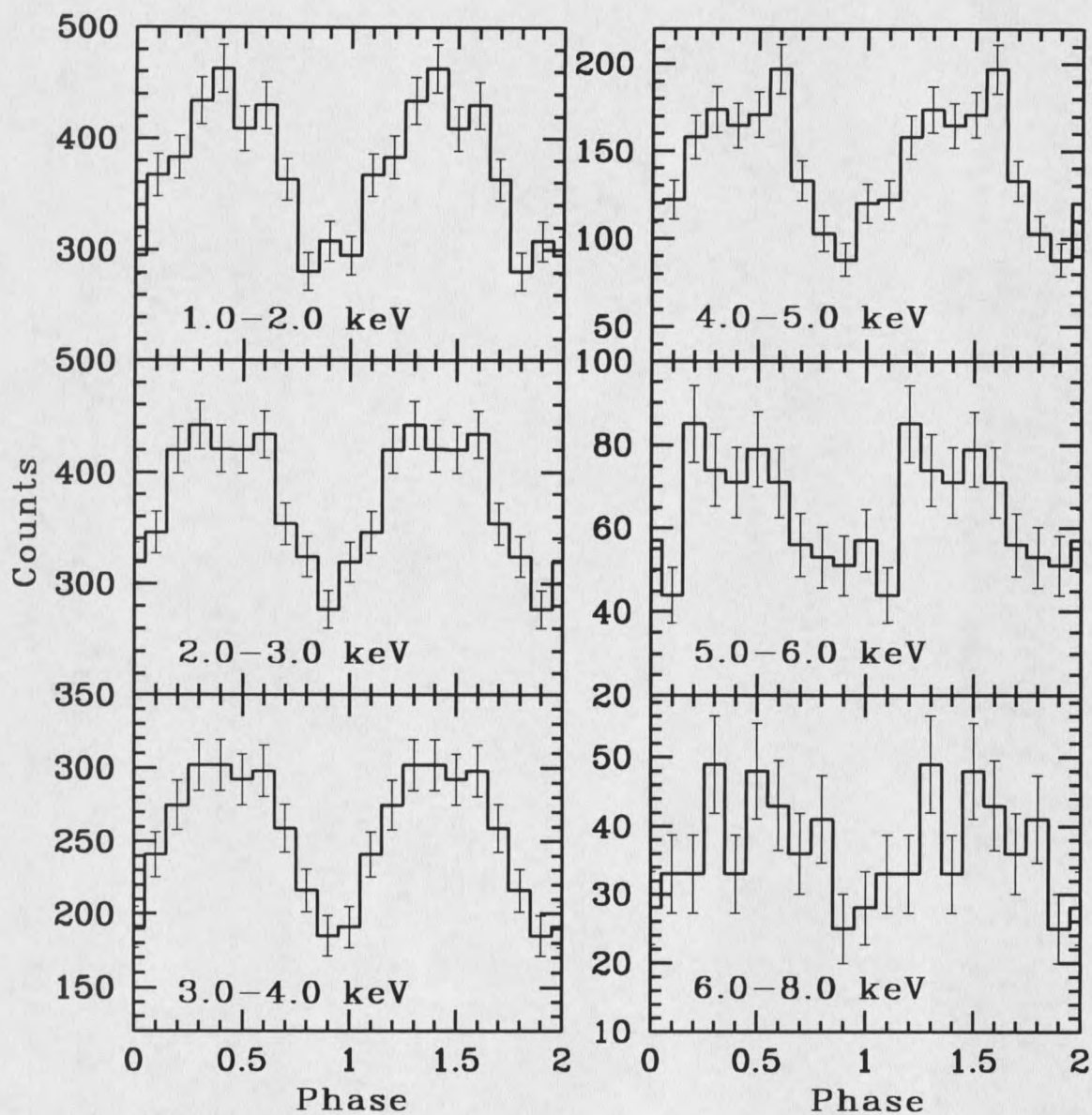


Figure 4.4: Energy resolved light curves for the first *Chandra* observation. There are insufficient counts below 1 keV and above 8 keV.

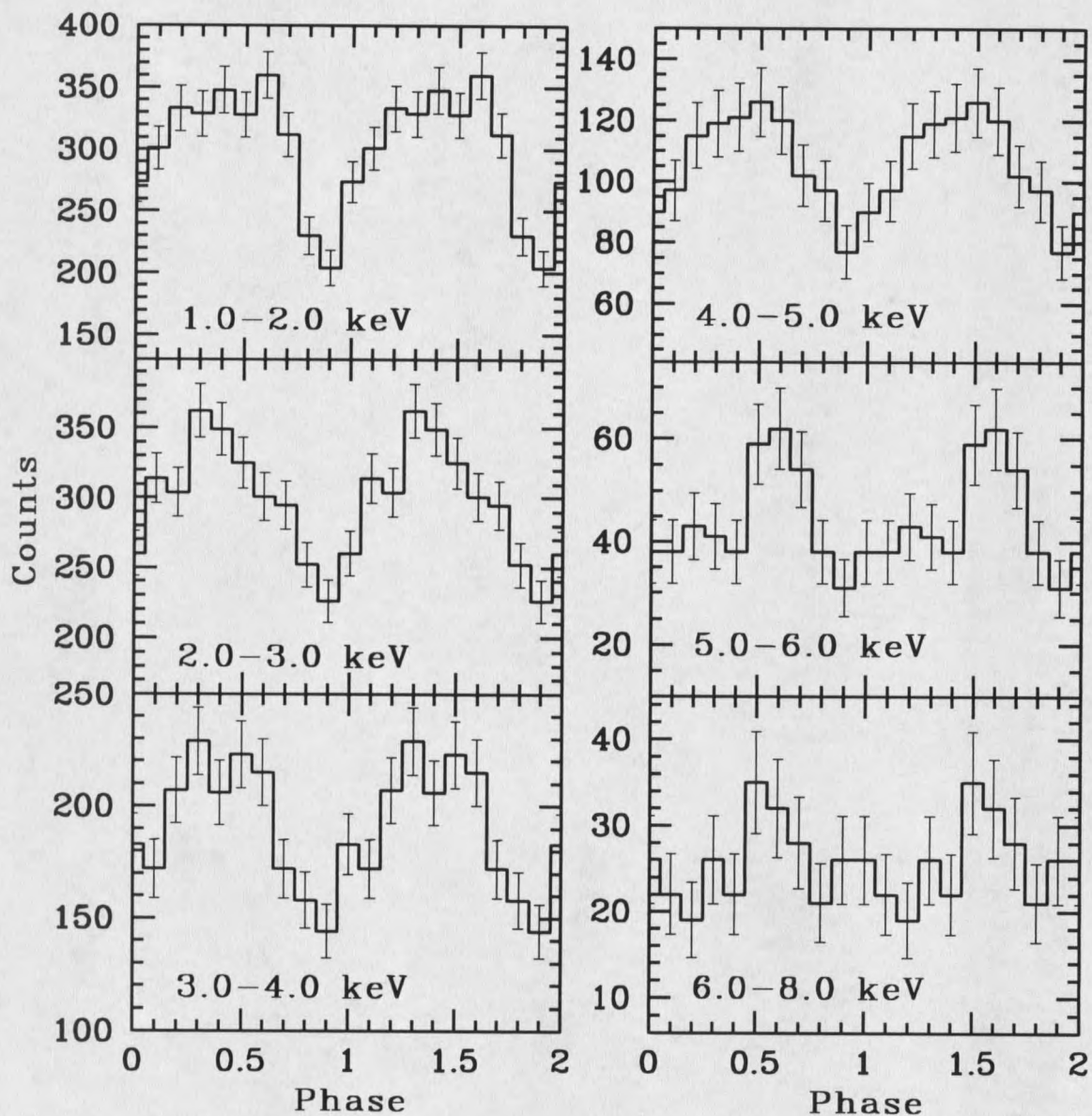


Figure 4.5: Energy resolved light curves for the second *Chandra* observation. The reduction of the observation time leads to an increase of uncertainty.

can be shown that  $S$  behaves as  $\chi^2$  so that the probability that two light curves are different depends on the value of  $S$ . The larger the result of  $S$ , the more probable that the two curves are different.

Using both the total light curve and the various schemes of energy resolved light curves, the maximum probability that we found for observation one differing from observation two was a little over 75%. Consequently, without a higher probability of difference, we regarded the light curves as the same, since there is still a 25% probability that they are indeed the same. We believe a more detailed statistical analysis should be done to determine if any differences can be extracted.

Our pulsed fraction calculations, however, suggested at least some difference between the two observations. Figure 4.6 shows our pulsed fractions as a function of energy for the two observations. We found a change in the fractional pulse for the two observations in the 4-5 keV range, suggesting that the more active state of the soft gamma ray repeater in the first observation has stronger pulsations in the 4-5 keV range than does the second observation. However, the uncertainty of our pulsed fraction overlaps slightly between the two observations making the change uncertain. We noted an interesting behavior present in the first observation that prevents the pulsed fraction from being constant over the entire energy range, as we found no horizontal line will pass through all the points in the top panel of figure 4.6.

Overall our timing analysis suggests that there is little difference in the light curves between the two observations, apart from the the overall flux and the pulsed fraction in the 4-5 keV range. For any differences to be apparent we left it to the phase

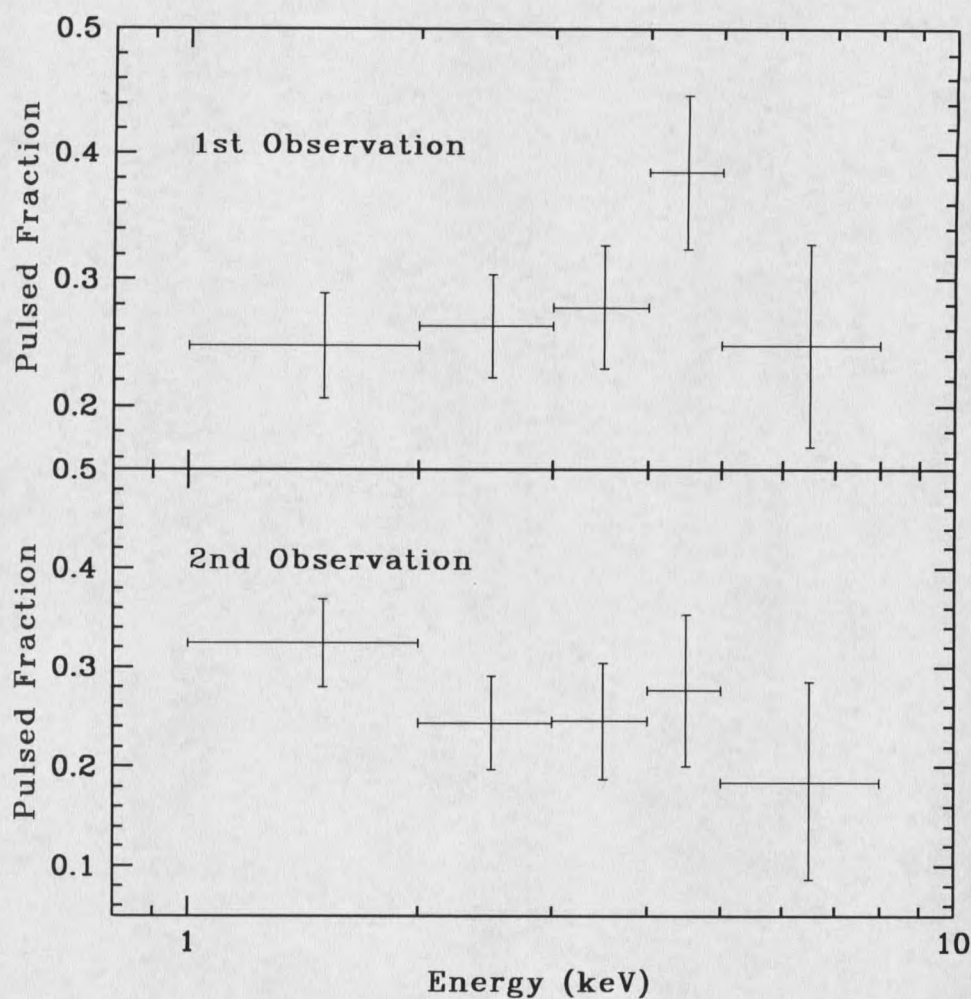


Figure 4.6: Energy resolved pulsed fraction for both of the *Chandra* observations. Notice the significant change in the 4-5 keV range.

resolved spectra to resolve them.

#### Our Phase Integrated Spectral Analysis

We found that a single blackbody does not fit the *Chandra* spectrum for either observation. In fact, the observations for the flare in the  $\gamma$ -rays suggests that some sort of power-law exists, which extends into the hard X-rays in the *RXTE* band.

Assuming that the power-law does continue to lower energy, we tried a single power-law model for both *Chandra* observations. Table 4.1 shows the results for a single power-law fit for both observations, and figure 4.7 shows our fit to the combined observation.

Table 4.1: Single power-law fit for both observations. The values in the parenthesis are best fit values using the fixed  $n_{H,22}$  value from the combined fit.

	Obs 1+2	Obs 1	Obs 2
$n_{H,22}$	$2.850^{+0.098}_{-0.095}$	$2.81^{+0.13}_{-0.12}$ (2.850)	$2.90^{+0.15}_{-0.14}$ (2.850)
$\Gamma$	$2.675^{+0.082}_{-0.080}$	$2.61 \pm 0.11$ ( $2.638^{+0.036}_{-0.037}$ )	$2.76^{+0.13}_{-0.12}$ ( $2.716 \pm 0.041$ )
$N_{\Gamma} 10^{-2} \text{ keV s}^{-1} \text{ cm}^{-2}$	$1.05^{+0.13}_{-0.11}$	$0.99^{+0.16}_{-0.14}$ ( $1.041^{+0.044}_{-0.043}$ )	$1.12^{+0.22}_{-0.18}$ ( $1.054^{+0.050}_{-0.049}$ )
$\chi^2$	445.5	226.7 (227.1)	193.4 (193.8)
$\chi^2_{\nu}$	1.119	1.030 (1.027)	1.105 (1.101)

Overall, we found that a single power-law fit works for both observations, as well as the combination of the two. A single power-law model, however, has a distinct difficulty in that it did not easily explain the pulsed fraction change that we found in the first observation. If only a power-law exists, we surmised that there are only two ways it could pulse. One was by changing its index, the other by changing its normalization. Even if both variations were present, we did not find a clear combination of the two which would fit the data, and match our pulsed fraction.

We attempted another model, a blackbody plus a power-law model, for both observations. Figure 4.8 shows our fit for this model. We kept the power-law an





























































































































